

**Optimizing immunoPET imaging of tumor PD-L1 expression: pharmacokinetic, biodistribution and dosimetric comparisons of <sup>89</sup>Zr-labeled anti-PD-L1 antibody formats**

Alizée Bouleau,<sup>1</sup> Hervé Nozach,<sup>2</sup> Steven Dubois,<sup>2</sup> Dimitri Kereselidze,<sup>1</sup> Céline Chevaleyre,<sup>1</sup> Cheng-I Wang,<sup>3</sup> Michael J. Evans,<sup>4</sup> Vincent Lebon,<sup>1</sup> Bernard Maillère,<sup>2</sup> Charles Truillet<sup>1</sup>.

<sup>1</sup>Paris-Saclay University, CEA, CNRS, Inserm, Multimodal Biomedical Imaging Lab (BioMaps), Orsay, France.

<sup>2</sup>Paris-Saclay University, CEA, INRAE, Medicines and Healthcare Technologies Department, SIMoS, Gif-sur-Yvette, France.

<sup>3</sup>Singapore Immunology Network, A\*STAR, Immunos, Singapore, Singapore.

<sup>4</sup>Department of Radiology and Biomedical Imaging, UCSF, San Francisco, CA, USA.

**Corresponding author**

Charles Truillet, PhD.

SHFJ, 4 place du Général Leclerc, 91401 Orsay, France.

Tel: 01 69 86 77 27

E-mail: [charles.truillet@universite-paris-saclay.fr](mailto:charles.truillet@universite-paris-saclay.fr)

**First author**

Alizée Bouleau, PhD student.

SHFJ, 4 place du Général Leclerc, 91401 Orsay, France.

E-mail: [alizee.bouleau@universite-paris-saclay.fr](mailto:alizee.bouleau@universite-paris-saclay.fr)

**Funding**

This work was funded by the Exploratory Program of the CEA and performed at an imaging platform supported by the France Life Imaging network (ANR-11-INBS-0006).

**Short running title**

Optimizing immunoPET imaging of PD-L1

**Word count**

4977

## Abstract

Positron emission tomography (PET) imaging of programmed cell death-ligand 1 (PD-L1) may help to non-invasively predict and monitor responses to anti-PD-1/anti-PD-L1 immunotherapies. In this study, we compared the imaging characteristics of three radioligands derived from the anti-PD-L1 IgG1 C4. In addition to the IgG C4, we produced a fragment antigen-binding (Fab) C4, and a double mutant IgG C4 (H310A/H435Q) with minimal affinity for the murine neonatal Fc receptor (FcRn). **Methods:** The pharmacokinetics (PK), biodistribution and dosimetry of the three <sup>89</sup>Zr-labeled C4 ligands were compared by longitudinal PET/CT imaging in nude mice bearing subcutaneous human non-small cell lung cancer (NSCLC) xenografts with positive (H1975 model) or negative (A549 model) endogenous PD-L1 expression. **Results:** The C4 radioligands substantially accumulated in PD-L1<sup>+</sup> tumors, but not in PD-L1<sup>-</sup> tumors or in blocked PD-L1<sup>+</sup> tumors, confirming their PD-L1-specific tumor targeting. <sup>89</sup>Zr-Fab C4 and <sup>89</sup>Zr-IgG C4 (H310A/H435Q) were rapidly eliminated compared to <sup>89</sup>Zr-IgG C4. Consequently, maximal tumor-to-muscle ratios (TMRs) were obtained earlier, at 4 h post-injection (p.i.) for <sup>89</sup>Zr-Fab C4 (TMR of ~6) and 24 h p.i. for <sup>89</sup>Zr-IgG C4 (H310A/H435Q) (TMR of ~9), versus 48 h p.i. for <sup>89</sup>Zr-IgG C4 (TMR of ~8). Background activity in non-tumor tissues was low, except for high kidney retention of <sup>89</sup>Zr-Fab C4 and persistent liver accumulation of <sup>89</sup>Zr-IgG C4 (H310A/H435Q) compared to <sup>89</sup>Zr-IgG C4. Dosimetry estimates suggested that the C4 radioligands would yield organ absorbed doses tolerable for repeated clinical PET imaging studies. **Conclusion:** This study highlights the potential of designing radioligands with shorter PK for PD-L1 immunoPET imaging in a preclinical model, and encourages further clinical translation of such radioligands.

**Keywords:** positron emission tomography (PET), programmed cell death-ligand 1 (PD-L1), immunotherapy, pharmacokinetics, non-small cell lung cancer (NSCLC).

## Introduction

Immunotherapies with monoclonal antibodies targeting the PD-1/PD-L1 immune checkpoint pathway have significantly improved the treatment of NSCLC (1,2). However, despite remarkable results observed in some NSCLC patients, only a small subset (~10-20%) actually responded to anti-PD-1/anti-PD-L1 immunotherapies (3). Therefore, reliable predictive biomarkers of response to PD-1/PD-L1 immune checkpoint inhibitors are urgently needed to guide patient stratification and to maximize therapeutic benefit (4).

PD-L1 expression in NSCLC tumors, determined by immunohistochemistry (IHC) on biopsied material, was associated with higher response rates to anti-PD-1/anti-PD-L1 immunotherapies (5,6). However, IHC evaluation of PD-L1 expression suffers from several limitations that might contribute to the discrepancies observed in treatment response (1). Notably, a single biopsy cannot reflect the spatiotemporal heterogeneity of PD-L1 expression within and across tumor lesions of a patient (4).

PET with radioligands targeting PD-L1 is a promising approach to complement the conventional IHC procedure, as it can provide a holistic, non-invasive, quantitative, and real-time assessment of PD-L1 expression (7). ImmunoPET combines the sensitivity of PET with the high specificity and affinity of radiolabeled antibodies or antibody-derived fragments. Clinical studies involving NSCLC patients have shown encouraging results regarding the predictive value of PD-L1 PET imaging for anti-PD-1/anti-PD-L1 immunotherapies (8,9). In addition of supporting patient selection, PD-L1 PET imaging may also assist in treatment monitoring and response evaluation, facilitating personalized immunotherapy treatments.

A wide range of radioligands targeting PD-L1 have been investigated in preclinical and clinical PET imaging studies (7). Many of these studies used the clinically-approved monoclonal antibodies atezolizumab or avelumab, radiolabeled with zirconium-89 (<sup>89</sup>Zr). However, smaller anti-PD-L1 PET radioligands have gained increasing interest. In contrast to full-length antibodies, they can rapidly and deeply diffuse into tumors while being quickly cleared from the blood. As a result, high-contrast images can be obtained within only hours after radioligand administration. Besides size reduction, another strategy for enhancing blood clearance of radiolabeled immunoglobulins G (IgGs) relies on altering their binding affinity to the FcRn (10). The FcRn is responsible for the extended plasmatic half-life of IgGs (~21 days), by protecting them from intracellular catabolism through the FcRn-mediated recycling pathway.

Introduction of mutations at key amino acid residues in the IgG Fc domain (e.g. I253, H310, H435) resulted in IgG variants with greatly decreased binding affinity to murine FcRn and significantly faster blood elimination in mice ([11–14](#)).

In this comparative study, we investigated two different approaches to design anti-PD-L1 PET radioligands with optimized PK properties. We produced a Fab fragment (50 kDa) derived from the antibody C4, a human recombinant IgG1 targeting both human and murine PD-L1. The <sup>89</sup>Zr-labeled IgG C4 was previously used for PD-L1 PET imaging in human NSCLC xenograft models and in a patient-derived xenograft model from a NSCLC patient ([15](#)). We also engineered a double mutant IgG C4 (H310A/H435Q) (150 kDa), with minimal affinity for the murine FcRn. The PK, biodistribution and dosimetry of the <sup>89</sup>Zr-labeled IgG C4, IgG C4 (H310A/H435Q) and Fab C4 were evaluated in human NSCLC xenograft models.

## **Materials and Methods**

### **Production of the C4 ligands**

The C4 IgG heavy and light chains were cloned into the AbVec2.0-IGHG1 and AbVec1.1-IGLC plasmids, respectively ([16](#)). For the Fab C4, the Fc fragment was replaced by a polyhistidine tag. Human HEK293 Freestyle cells (Thermo-Fisher) ( $2.5 \times 10^6$  cells/mL) were transiently co-transfected in 100 mL of Freestyle medium (Thermo-Fisher) by adding 150 µg of each plasmid and 1.8 mL of linear polyethylenimine (0.5 mg/mL, Polysciences). Cells were incubated for 7 days at 37°C, 120 rpm, 8% CO<sub>2</sub>. The culture supernatant was purified using HiTrap Protein A, Lambda FabSelect or HisTrap Excel columns (GE Healthcare) for IgG C4, IgG C4 (H310A/H435Q) and Fab C4, respectively. Size-exclusion chromatography was performed using Sephacryl-S-200 HR columns (Sigma) with PBS.

### **Bio-layer interferometry**

Binding kinetics of the C4 ligands to human PD-L1 (Sinobiological) were determined by bio-layer interferometry (BLI) using an Octet RED96 instrument (ForteBio). Anti-hIgG Fc Capture Biosensors (ForteBio) were loaded with the IgGs C4 (50 nM) for 60 s. Association of human PD-L1 was measured at different concentrations (1.6 nM-100 nM) for 300 s, before dissociation for 1000 s in kinetic buffer (PBS with 0.5% BSA and 0.05% Tween 20).

Streptavidin Biosensors (Fortebio) were loaded with biotinylated human PD-L1 (50 nM) for 60 s. Association of Fab C4 was measured at different concentrations (0.78 nM-6.3 nM) for 200 s, before dissociation for 1000 s in kinetic buffer. Binding curves were fitted to a global 1:1 binding model.

### **Radiolabeling**

The C4 ligands were conjugated with p-isothiocyanatobenzylferrioxamine (p-NCS-Bz-DFO, Macrocyclics) and radiolabeled with  $^{89}\text{Zr}$  (PerkinElmer) according to a previously published protocol (17). A 4-fold molar excess of p-NCS-Bz-DFO was added to 1 mL of C4 ligand solution (5 mg/mL), and reaction mixture was incubated for 45 min at 37°C. The DFO-C4 ligand conjugates were purified with a PD-10 column (GE Healthcare) using a gentisic acid solution. The DFO-C4 ligand solution was incubated with  $^{89}\text{Zr}$  (111 MBq) for 1 h at 37°C. The  $^{89}\text{Zr}$ -DFO-C4 ligand conjugates were purified with a PD-10 column using a gentisic acid solution, before being further concentrated and buffer exchanged in HEPES with a Vivaspin centrifugal concentrator (Sartorius). Radiochemical purity was assessed by instant thin layer chromatography and size-exclusion high-performance liquid chromatography.

### **Cell culture**

The human NSCLC cell lines H1975 and A549 were purchased from the American Type Culture Collection. Cells were cultured in RPMI-1640 medium (Gibco) for H1975 cells or Dulbecco's Modified Eagle's medium (Gibco) for A549 cells, supplemented with 10% fetal bovine serum (Gibco) and 1% antibiotic-antimycotic solution (Gibco), at 37°C in a humidified atmosphere with 5%  $\text{CO}_2$ .

### **Cell binding assays**

H1975 cells (2 million cells) were mixed with  $^{89}\text{Zr}$ -IgG C4,  $^{89}\text{Zr}$ -IgG C4 (H310A/H435Q) or  $^{89}\text{Zr}$ -Fab C4 (2 pmol, 4-8  $\mu\text{Ci}$ ), with or without a 100X molar excess of non-radiolabeled C4 ligand. The reaction mixture was incubated for 2 h at 37°C. Cell-associated activity was measured with the Wizard<sup>2</sup> gamma counter (PerkinElmer) and expressed as percentage of the total activity added per sample.

## **Immunoblotting**

Total proteins (30 µg) from whole-cell lysates were separated by electrophoresis on Mini-PROTEAN TGX gels (Bio-Rad) and transferred over to a polyvinylidene fluoride membrane (Merck Millipore). Blots were incubated with the following primary antibodies: rabbit anti-human PD-L1 (1:1000, clone E1L3N, Cell Signaling) and rabbit anti-human  $\alpha$ -tubulin (1:1000, Cell Signaling). Blots were then incubated with an HRP-conjugated donkey anti-rabbit secondary antibody (1:10,000, Jackson ImmunoResearch). Proteins were detected using the Clarity Western ECL Substrate (Bio-Rad). Immunoblots were imaged with the FUSION FX imaging system (Vilber).

## **Animals**

Animal experiments were performed according to the European Directive 2010/63/EU and to its transposition into the French law (Decree No. 2013-118). The research project was conducted at the CEA-SHFJ imaging platform (authorization D91-471-105) and was approved by a local ethics committee (CETEA-CEA DSV IdF). Female nude mice (NMRI-FOXN1 Nu/Nu, Janvier) were housed in individually-ventilated cages in a temperature (22°C) and humidity (40%)-controlled room, with a 12-h light/12-h dark cycle. Animal experiments were performed under anesthesia with isoflurane in oxygen.

## **Subcutaneous injections**

Anesthetized mice were subcutaneously inoculated in both lower flanks with H1975 or A549 cells ( $4-5 \times 10^6$  cells) suspended in PBS/Matrigel (BD Biosciences) (1:1). Mice were used for PET imaging studies when tumors reached ~8 mm at the largest diameter.

## **microPET/CT imaging**

Mice ( $10 \pm 1$  weeks,  $27.8 \pm 1.4$  g) were intravenously injected with the  $^{89}\text{Zr}$ -labeled C4 ligands ( $3.7 \pm 0.7$  MBq,  $7.0 \pm 3.0$  MBq/nmol,  $0.6 \pm 0.3$  nmol). For blocking studies, mice were co-injected with a 20X molar excess of non-radiolabeled C4 ligands (1.2 nmol). PET emission scans were performed using an Inveon microPET scanner and an Inveon microPET/CT scanner (Siemens). A 60-min dynamic PET scan was performed immediately after radioligand injection. 20-min static PET scans were subsequently acquired at selected times (4 h, 24 h, 48 h, 72 h and 7 days)

post-injection (p.i.). After each PET scan, a transmission scan or a CT scan was performed for photon attenuation correction. PET images were reconstructed with the Inveon Acquisition Workspace software (v2.1) using the OP-OSEM3D-MAP algorithm. Normalization and corrections for dead-time, scatter, decay and attenuation were applied to all PET data. Volumes of interest (VOIs) were defined with the PMOD software (v3.9). Fixed-size spherical VOIs (3.5-8 mm<sup>3</sup>) were drawn in representative parts of the heart, liver and kidneys. Mouse whole-body, spleen and subcutaneous tumors were delineated semi-automatically. The mean activity concentration (kBq/cm<sup>3</sup>) in each VOI was divided by the total injected dose (kBq) to obtain the percentage of injected dose per volume of tissue (%ID/cm<sup>3</sup>).

### **Immunohistochemistry**

Fixed frozen tumor sections (12 μm) were incubated with a rabbit anti-human PD-L1 primary antibody (1:100, clone E1L3N, Cell Signaling). Slides were then incubated with an HRP-conjugated donkey anti-rabbit secondary antibody (1:500, Jackson ImmunoResearch). Peroxidase activity was detected with 3-3'-Diaminobenzidine (DAB) (BD Pharmingen). Tumor sections were counterstained with Harris hematoxylin (Sigma-Aldrich). Standard hematoxylin and eosin (H&E) staining was performed on adjacent tumor sections. Images of stained tumor sections were acquired with the Axio Observer 5 microscope (Zeiss).

### **Flow cytometry**

Single-cell suspensions were incubated with the following fluorescent-labeled antibodies (10 μg/mL): PE-conjugated anti-human PD-L1 antibody (clone 29E.2A3, BioLegend) and PE-conjugated mouse IgG2b, κ isotype control (clone MPC-11, BioLegend). For viability assessment, cells were incubated with the Zombie Green viability dye (1:500, BioLegend). Flow cytometry acquisitions were performed on the Attune NxT Acoustic Focusing Cytometer (Invitrogen). Data were analyzed with FlowJo (v10.7).

### **Blood pharmacokinetics**

Plasma activity concentrations were calculated from image-derived blood pool activity concentrations. Considering that antibodies are restricted to the plasma, a blood-to-plasma concentration ratio of 0.55 was used. For

each C4 radioligand, plasma time-activity curves of individual mice were pooled together and fitted to a two-compartment model with the NONMEM software (v6.2).

## Dosimetry

For each C4 radioligand, residence times ( $\text{kBq}\cdot\text{h}\cdot\text{kBq}^{-1}$ ) in main source organs (blood pool, liver, kidneys, spleen, remainder of the body) of individual mice were derived from longitudinal PET images and used in the IDAC-Dose software (v2.1) (18) for human dosimetry estimations. Murine dosimetry was also performed (Supplemental Table 1) (19).

## Statistics

Statistical analyses were performed with GraphPad Prism (v9.0.1). A two-tailed Student t test was used for two-group data comparison (\*  $P < 0.05$ , \*\*  $P < 0.01$ , \*\*\*  $P < 0.001$ , \*\*\*\*  $P < 0.0001$ ).

## Results

### Production and characterization of the C4 radioligands

BLI measurements showed that IgG C4, IgG C4 (H310A/H435Q) and Fab C4 displayed high binding affinities for human PD-L1, with nanomolar affinity constants ( $K_D$ ) (Supplemental Figure 1, Supplemental Table 2). The three C4 ligands were successfully conjugated to p-NCS-Bz-DFO and subsequently radiolabeled with  $^{89}\text{Zr}$ . Radiochemical purity exceeded 95% in all radiosynthesis experiments ( $N = 6$ ) (Supplemental Figure 2, Supplemental Table 3). Endogenous PD-L1 expression on H1975 and A549 cells was confirmed by immunoblotting and flow cytometry (Figure 1). H1975 cells exhibited high PD-L1 expression compared to A549 cells, with median fluorescence intensity (MFI) values of  $713 \pm 56$  and  $107 \pm 7$ , respectively. *In vitro* binding assays showed that binding of the  $^{89}\text{Zr}$ -labeled C4 ligands to PD-L1<sup>+</sup> H1975 cells was significantly blocked (>70% reduction) by co-incubation with an excess of non-radiolabeled ligands, demonstrating their PD-L1 binding specificity of the C4 radioligands (Figure 1).

### microPET/CT imaging with the C4 radioligands in a PD-L1<sup>+</sup> human NSCLC xenograft model

Female nude mice bearing subcutaneous PD-L1<sup>+</sup> H1975 xenografts were injected with the C4 radioligands ( $3.7 \pm 0.7$  MBq,  $0.6 \pm 0.3$  nmol) and longitudinal microPET/CT imaging was performed (Supplemental Figures 3, 4, 5 and 6, Supplemental Tables 4 and 5).

Various blood PK parameters of the C4 radioligands were estimated (Table 1, Supplemental Figure 7). The <sup>89</sup>Zr-Fab C4 fragment exhibited the fastest blood clearance. The Fc-mutant <sup>89</sup>Zr-IgG C4 (H310A/H435Q) was also rapidly cleared from circulation as compared to the wild-type (WT) <sup>89</sup>Zr-IgG C4, with a 3.4x superior systemic clearance (CL). Remarkably, the estimated biologic elimination half-lives ( $t_{1/2\beta}$ ) were similar for <sup>89</sup>Zr-IgG C4 and <sup>89</sup>Zr-IgG C4 (H310A/H435Q). This may be explained by the higher retention of <sup>89</sup>Zr-IgG C4 (H310A/H435Q) in the peripheral compartment, as shown by its smaller distribution rate constant from peripheral to central compartment ( $k_{21}$ ) compared to that of <sup>89</sup>Zr-IgG C4.

The three C4 radioligands were able to effectively detect PD-L1 expression in H1975 xenografts, but with different tumor uptakes and kinetics (Figure 2). For <sup>89</sup>Zr-IgG C4, optimal PET images were observed at 48 h p.i. with highest tumor uptake ( $C_{\max}$ ) of  $4.85 \pm 0.61$  %ID/cm<sup>3</sup>, maximal tumor-to-muscle ratio ( $TMR_{\max}$ ) of  $8.34 \pm 0.63$ , and tumor-to-blood ratio (TBR) of  $0.84 \pm 0.35$ . <sup>89</sup>Zr-IgG C4 (H310A/H435Q) tumor accumulation peaked at 24 h p.i., with  $C_{\max}$  and  $TMR_{\max}$  values similar to those obtained with the <sup>89</sup>Zr-IgG C4 ( $4.60 \pm 0.39$  %ID/cm<sup>3</sup> and  $9.39 \pm 0.36$ ) and a TBR of  $2.20 \pm 1.21$ . Maximal tumor uptake of <sup>89</sup>Zr-Fab C4 was observed even earlier at 4 h p.i.. However,  $C_{\max}$  ( $1.36 \pm 0.11$  %ID/cm<sup>3</sup>) and  $TMR_{\max}$  ( $6.28 \pm 0.24$ ) values were substantially lower, even if the TBR was still  $1.53 \pm 0.85$ . For the three C4 radioligand, H1975 tumor uptake was significantly reduced in mice that received a blocking dose of cold C4 ligand (Figure 3, Supplemental Table 6), suggesting their PD-L1-specific tumor targeting.

Background activity in most normal tissues was low (Figure 2). Whereas <sup>89</sup>Zr-IgG C4 liver uptake gradually decreased over the imaging time course, <sup>89</sup>Zr-IgG C4 (H310A/H435Q) demonstrated high and persistent liver accumulation. The <sup>89</sup>Zr-Fab C4 fragment essentially accumulated in the kidneys. This high renal signal retention precluded spleen detection on PET images, and <sup>89</sup>Zr-Fab C4 spleen uptake was therefore not quantified.

For each C4 radioligand, human organ absorbed dose estimates were extrapolated from murine longitudinal biodistribution data. The highest absorbed doses were observed in the kidneys and adrenals for <sup>89</sup>Zr-Fab C4, and in the liver and heart wall for <sup>89</sup>Zr-IgG C4 and <sup>89</sup>Zr-IgG C4 (H310A/H435Q) (Supplemental Table 7). The estimated

effective doses were of  $0.34 \pm 0.03$ ,  $0.35 \pm 0.02$  and  $0.26 \pm 0.05$  mSv/MBq for  $^{89}\text{Zr}$ -IgG C4,  $^{89}\text{Zr}$ -IgG C4 (H310A/H435Q), and  $^{89}\text{Zr}$ -Fab C4, respectively.

#### **microPET/CT imaging with the C4 radioligands in PD-L1<sup>+</sup> and PD-L1<sup>-</sup> human NSCLC xenograft models**

The ability of  $^{89}\text{Zr}$ -IgG C4 to discriminate between various tumor PD-L1 expression levels was previously demonstrated (15).  $^{89}\text{Zr}$ -IgG C4 (H310A/H435Q) and  $^{89}\text{Zr}$ -Fab C4 effectively accumulated in PD-L1<sup>+</sup> H1975 xenografts, but not in PD-L1<sup>-</sup> A549 xenografts (Figure 4, Supplemental Figure 8, Supplemental Table 8). For both radioligands, maximal tumor uptakes were ~2-fold higher in H1975 tumors versus A549 tumors. PD-L1 IHC showed heterogeneous PD-L1 staining in H1975 tumor sections, whereas very little/no PD-L1 staining was detected in A549 tumor sections (Figure 4). Flow cytometry corroborated the IHC results, with PD-L1-associated MFI values of  $223.9 \pm 34.7$  versus  $72.1 \pm 2.5$  for the H1975 and A549 tumor cells, respectively (Figure 4, Supplemental Figure 9). These *ex vivo* analyses further validated the *in vivo* PD-L1-specific tumor targeting of  $^{89}\text{Zr}$ -IgG C4 (H310A/H435Q) and  $^{89}\text{Zr}$ -Fab C4.

#### **Discussion**

The three C4 radioligand formats exhibited marked differences in kinetics and *in vivo* biodistribution patterns, but they were all able to detect PD-L1 expression in human NSCLC xenografts. Although rapid elimination of the  $^{89}\text{Zr}$ -Fab C4 fragment gave high contrast images as soon as 4 h p.i., it also resulted in a poor maximal tumor uptake. Nonetheless, this tumor uptake was similar to that obtained in other preclinical studies performing same-day PET imaging with small anti-PD-L1 radioligands, such as the fluorine-18 ( $^{18}\text{F}$ )-labeled adnectin BMS-986192 or small peptide WL12 (20–23). The faster blood clearance of the Fc-mutant  $^{89}\text{Zr}$ -IgG C4 also enabled earlier lesion detection compared to the WT  $^{89}\text{Zr}$ -IgG C4. Unlike  $^{89}\text{Zr}$ -Fab C4, the decreased background signal was not accompanied by a reduced tumor uptake, that remained similar to that of  $^{89}\text{Zr}$ -IgG C4. In contrast to the monovalent Fab C4, the Fc-mutant IgG C4 retains two binding sites, hence maintaining a strong avidity for tumoral PD-L1. Anti-PD-L1 radioligands with low background activity facilitate the detection of low tumor PD-L1 expression levels. This is particularly relevant for clinical PD-L1 PET imaging, as patients with only 1% of PD-L1<sup>+</sup> tumor cells can generate higher response rates to anti-PD-1/PD-L1 immunotherapies than patients with PD-L1<sup>-</sup> tumors (6). Moreover, the

H310A/H435Q double mutation has a translational interest because IgG1 binding to human FcRn also involves the conserved H310 and H435 residues (10,14).

Liver accumulation of the <sup>89</sup>Zr-labeled IgGs C4 was consistent with primary clearance of antibodies through the hepatobiliary system. The increased liver retention obtained with the Fc-mutant <sup>89</sup>Zr-IgG C4 was also observed in other preclinical studies that altered the interaction of indium-111 (<sup>111</sup>In)-labeled IgG1s with the murine FcRn (13,24,25). For instance, Yip *et al.* generated a mutated variant (H310Q) of a humanized IgG1 with greatly decreased binding affinity to murine FcRn. In immunocompetent mice, liver radioactivity uptake of the <sup>111</sup>In-IgG1 (H310Q) at 24 h post-injection was ~2x higher than that of the parental <sup>111</sup>In-IgG1 (13). These results suggested that, in the absence of FcRn protection, the liver emerged as a major site of IgG catabolism in mice.

The <sup>89</sup>Zr-Fab C4 fragment was small enough to primarily undergo renal clearance (26). The intense signal retention in the kidneys may be due to the re-absorption of the radiolabeled Fab C4 fragment by proximal tubular cells following glomerular filtration. Several strategies have been implemented to reduce such renal accumulation of small radioligands, including co-infusion of basic amino acids that compete with the radioligand for tubular reabsorption (27). PET imaging with the <sup>89</sup>Zr-Fab C4 fragment may be particularly adapted for detection of PD-L1 expression in tumor lesions within abdominal organs, that would otherwise be obstructed by the liver clearance signal of the <sup>89</sup>Zr-IgGs C4. This is especially relevant for PD-L1 immunoPET imaging in NSCLC patients, as they are often diagnosed at advanced stages with multiple distant metastases already spread. Approximately 17% of NSCLC patients will develop metastasis in the liver (28).

As we used immunocompromised mice in this study, the impact of endogenous PD-L1 expression in normal tissues (e.g. lymphoid tissues such as the spleen) on biodistribution and tumor-targeting of the C4 radioligands could not be properly evaluated. Thanks to its cross-reactivity with murine PD-L1, the <sup>89</sup>Zr-labeled IgG C4 has already been evaluated in a syngeneic mouse model of melanoma (B16-F10) (15). Surprisingly, no notable differences in radioligand uptake within normal tissues were observed between the B16-F10 tumor-bearing immunocompetent mice and the H1975 tumor-bearing immunocompromised mice.

The estimated human effective doses for the three C4 radioligands were in the same range as the values obtained in clinical immunoPET studies using other  $^{89}\text{Zr}$ -labeled antibodies. Administration of 37 MBq in patients, as already performed in a clinical study with  $^{89}\text{Zr}$ -atezolizumab (8), would result in effective doses of  $\sim 13$  mSv for the  $^{89}\text{Zr}$ -IgGs C4 and of  $\sim 10$  mSv for the  $^{89}\text{Zr}$ -Fab C4. By comparison, the effective dose of a  $^{18}\text{F}$ -fluorodeoxyglucose ( $^{18}\text{F}$ -FDG) PET scan is  $\sim 6$ -7 mSv (29). The favorable dosimetry of the C4 radioligands may enable repeated PD-L1 immunoPET imaging, as it would be required for treatment response monitoring. Moreover, thanks to its faster PK, the Fab C4 may be radiolabeled with a shorter-lived PET isotope such as  $^{18}\text{F}$ , which would minimize the patient radiation burden.

## **Conclusion**

The  $^{89}\text{Zr}$ -labeled Fab C4 fragment and Fc-mutant IgG C4 enabled to specifically and efficiently detect PD-L1 expression in a human NSCLC xenograft model at earlier time points than the parental  $^{89}\text{Zr}$ -labeled IgG C4. This study demonstrated the feasibility of designing anti-PD-L1 radioligands with enhanced imaging characteristics for PD-L1 immunoPET imaging in preclinical models, and supports the clinical translation of such engineering approaches.

## **Disclosure**

This work was funded by the Exploratory Program of the CEA and performed at an imaging platform supported by the France Life Imaging network (ANR-11-INBS-0006). No potential conflicts of interest relevant to this article exist.

## **Acknowledgments**

We thank Jean-Marc Bertho and Sébastien Jan for their support on the dosimetry analysis. The graphical abstract was created with BioRender.com.

## **Key points**

**Question:** How to optimize immunoPET imaging of PD-L1 expression in NSCLC patients ?

**Pertinent findings:** A Fab fragment, and a double mutant IgG (H310A/H435Q) with minimal affinity for murine FcRn, were derived from the anti-PD-L1 IgG1 C4. The <sup>89</sup>Zr-labeled Fab C4 and IgG C4 (H310A/H435Q) enabled to effectively detect PD-L1 expression by PET imaging in a human NSCLC xenograft model, at earlier time points than the parental <sup>89</sup>Zr-labeled IgG C4.

**Implications for patient care:** These results highlight the possibility of designing anti-PD-L1 PET radioligands with optimized PK properties, in order to better predict and monitor responses to anti-PD-1/anti-PD-L1 immunotherapies with PD-L1 immunoPET.

## References

1. Constantinidou A, Alifieris C, Trafalis DT. Targeting Programmed Cell Death -1 (PD-1) and Ligand (PD-L1): a new era in cancer active immunotherapy. *Pharmacol Ther.* 2019;194:84-106.
2. Yang C-Y, Yang JC-H, Yang P-C. Precision management of advanced non-small cell lung cancer. *Annu Rev Med.* 2020;71:117-136.
3. Sun C, Mezzadra R, Schumacher TN. Regulation and function of the PD-L1 checkpoint. *Immunity.* 2018;48:434-452.
4. Nishino M, Ramaiya NH, Hatabu H, Hodi FS. Monitoring immune-checkpoint blockade: response evaluation and biomarker development. *Nat Rev Clin Oncol.* 2017;14:655-668.
5. Passiglia F, Bronte G, Bazan V, et al. PD-L1 expression as predictive biomarker in patients with NSCLC: a pooled analysis. *Oncotarget.* 2016;7:19738-19747.
6. Herbst RS, Baas P, Kim D-W, et al. Pembrolizumab versus docetaxel for previously treated, PD-L1-positive, advanced non-small-cell lung cancer (KEYNOTE-010): a randomised controlled trial. *The Lancet.* 2016;387:1540-1550.
7. Bouleau A, Lebon V, Truillet C. PET imaging of immune checkpoint proteins in oncology. *Pharmacol Ther.* 2021;222:107786.
8. Bensch F, van der Veen EL, Lub-de Hooge MN, et al. <sup>89</sup>Zr-atezolizumab imaging as a non-invasive approach to assess clinical response to PD-L1 blockade in cancer. *Nat Med.* 2018;24:1852-1858.
9. Niemeijer AN, Leung D, Huisman MC, et al. Whole body PD-1 and PD-L1 positron emission tomography in patients with non-small-cell lung cancer. *Nat Commun.* 2018;9:4664.
10. Pyzik M, Sand KMK, Hubbard JJ, Andersen JT, Sandlie I, Blumberg RS. The Neonatal Fc Receptor (FcRn): a misnomer? *Front Immunol.* 2019;10:1540.
11. Kim J-K, Firan M, Radu CG, Kim C-H, Ghetie V, Ward ES. Mapping the site on human IgG for binding of the MHC class I-related receptor, FcRn. *Eur J Immunol.* 1999;29:2819-2825.
12. Kenanova V, Olafsen T, Crow DM, et al. Tailoring the pharmacokinetics and positron emission tomography imaging properties of anti-carcinoembryonic antigen single-chain Fv-Fc antibody fragments. *Cancer Res.* 2005;65:622-631.
13. Yip V, Palma E, Tesar DB, et al. Quantitative cumulative biodistribution of antibodies in mice: effect of modulating binding affinity to the neonatal Fc receptor. *mAbs.* 2014;6:689-696.
14. Burvenich IJG, Parakh S, Lee F-T, et al. Molecular imaging of T cell co-regulator factor B7-H3 with <sup>89</sup>Zr-DS-5573a. *Theranostics.* 2018;8:4199-4209.
15. Truillet C, Oh HLJ, Yeo SP, et al. Imaging PD-L1 expression with immunoPET. *Bioconjug Chem.* 2018;29:96-103.
16. Smith K, Garman L, Wrammert J, et al. Rapid generation of fully human monoclonal antibodies specific to a vaccinating antigen. *Nat Protoc.* 2009;4:372-384.

17. Vosjan MJWD, Perk LR, Visser GWM, et al. Conjugation and radiolabeling of monoclonal antibodies with zirconium-89 for PET imaging using the bifunctional chelate p-isothiocyanatobenzyl-desferrioxamine. *Nat Protoc.* 2010;5:739-743.
18. Andersson M, Johansson L, Eckerman K, Mattsson S. IDAC-Dose 2.1, an internal dosimetry program for diagnostic nuclear medicine based on the ICRP adult reference voxel phantoms. *EJNMMI Res.* 2017;7:88.
19. Locatelli M, Miloudi H, Autret G, et al. RODES software for dose assessment of rats and mice contaminated with radionuclides. *J Radiol Prot.* 2017;37:214-229.
20. Wei J, Wang Y, Lee CY, et al. An analysis of isoclonal antibody formats suggests a role for measuring PD-L1 with low molecular weight PET radiotracers. *Mol Imaging Biol.* 2020;22:1553-1561.
21. Donnelly DJ, Smith RA, Morin P, et al. Synthesis and biologic evaluation of a novel <sup>18</sup>F-labeled adnectin as a PET radioligand for imaging PD-L1 expression. *J Nucl Med.* 2018;59:529-535.
22. Stutvoet TS, van der Veen EL, Kol A, et al. Molecular imaging of PD-L1 expression and dynamics with the adnectin-based PET tracer <sup>18</sup>F-BMS-986192. *J Nucl Med.* 2020;61:1839-1844.
23. Lesniak WG, Mease RC, Chatterjee S, et al. Development of [<sup>18</sup>F]FPy-WL12 as a PD-L1sSpecific PET imaging peptide. *Mol Imaging.* 2019;18:153601211985218.
24. Singh Jaggi J, Carrasquillo JA, Seshan SV, et al. Improved tumor imaging and therapy via i.v. IgG-mediated time-sequential modulation of neonatal Fc receptor. *J Clin Invest.* 2007;117:2422-2430.
25. Kenanova V, Olafsen T, Williams LE, et al. Radioiodinated versus radiometal-labeled anti-carcinoembryonic antigen single-chain Fv-Fc antibody fragments: optimal pharmacokinetics for therapy. *Cancer Res.* 2007;67:718-726.
26. Xenaki KT, Oliveira S, van Bergen en Henegouwen PMP. Antibody or antibody fragments: implications for molecular imaging and targeted therapy of solid tumors. *Front Immunol.* 2017;8:1287.
27. Vegt E, de Jong M, Wetzels JFM, et al. Renal toxicity of radiolabeled peptides and antibody fragments: mechanisms, impact on radionuclide therapy, and strategies for prevention. *J Nucl Med.* 2010;51:1049-1058.
28. Zhu T, Bao X, Chen M, et al. Mechanisms and future of non-small cell lung cancer metastasis. *Front Oncol.* 2020;10:585284.
29. Martí-Climent JM, Prieto E, Morán V, et al. Effective dose estimation for oncological and neurological PET/CT procedures. *EJNMMI Res.* 2017;7:37.

**Figures and Table**

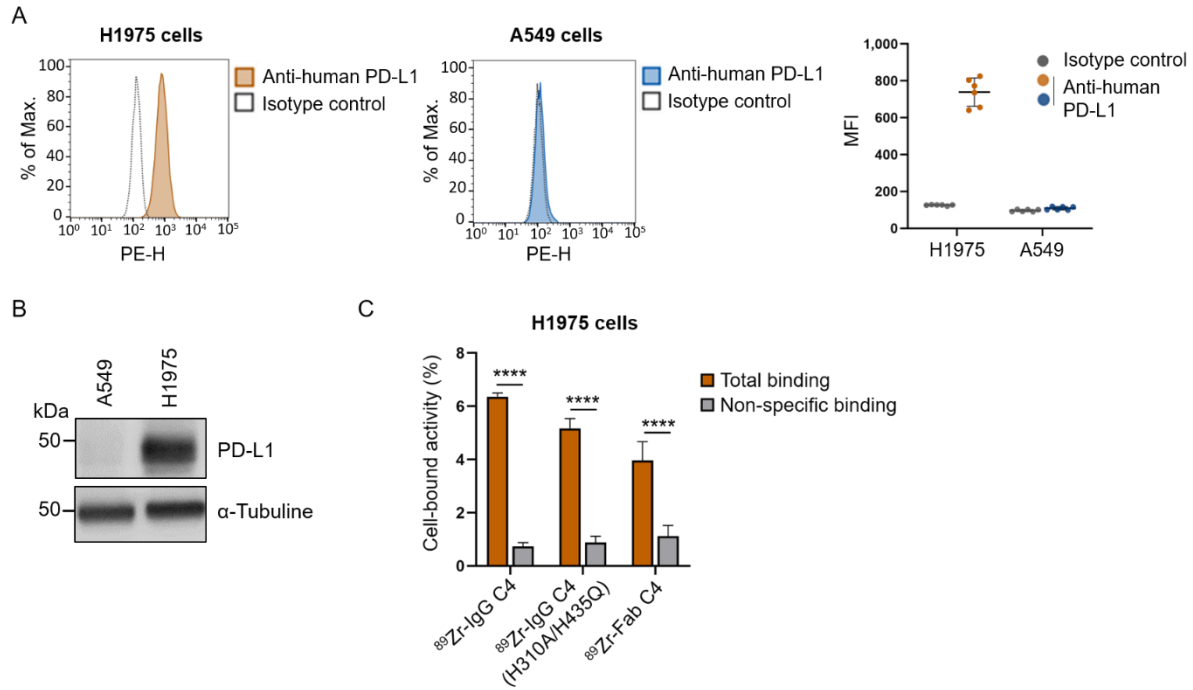


**Figure 1. Characterization of *in vitro* PD-L1 expression in human NSCLC cell lines and cell binding assays with the C4 radioligands.** (A) Representative flow cytometry histograms for cell-surface PD-L1 expression. MFI values are shown on the dot plot (N = 6 independent experiments/cell line). (B) Representative immunoblot image showing total PD-L1 expression in whole-cell lysates (C) Total and non-specific C4 radioligand binding to PD-L1<sup>+</sup> H1975 cells. Data are presented as mean ± SD, N = 6 replicates/condition. A two-tailed paired Student t test was used for data comparison. MFI: median fluorescence intensity, PE: phycoerythrin.

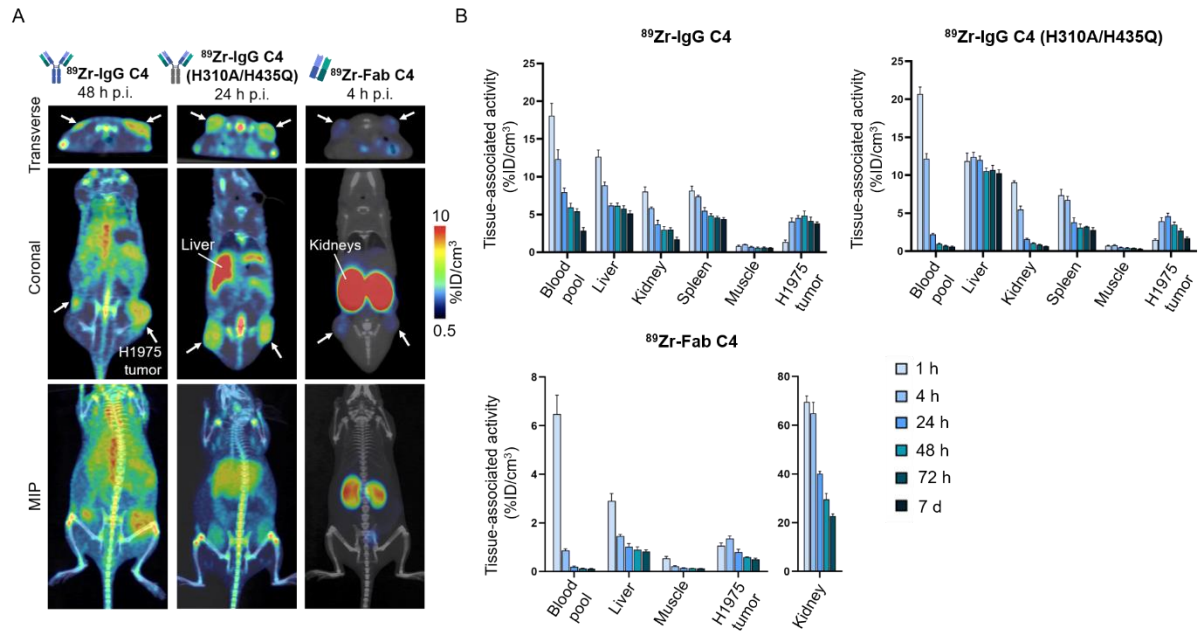


**Figure 2. microPET/CT imaging with the C4 radioligands in a PD-L1<sup>+</sup> human NSCLC xenograft model. (A)** Representative microPET/CT image sections and MIP images of mice bearing PD-L1<sup>+</sup> H1975 xenografts (white arrows). **(B)** Image-derived *in vivo* biodistribution of the C4 radioligands. Data are presented as mean  $\pm$  SD, N = 6 mice/group. MIP: maximum intensity projection, %ID/cm<sup>3</sup>: percentage injected dose per volume of tissue.

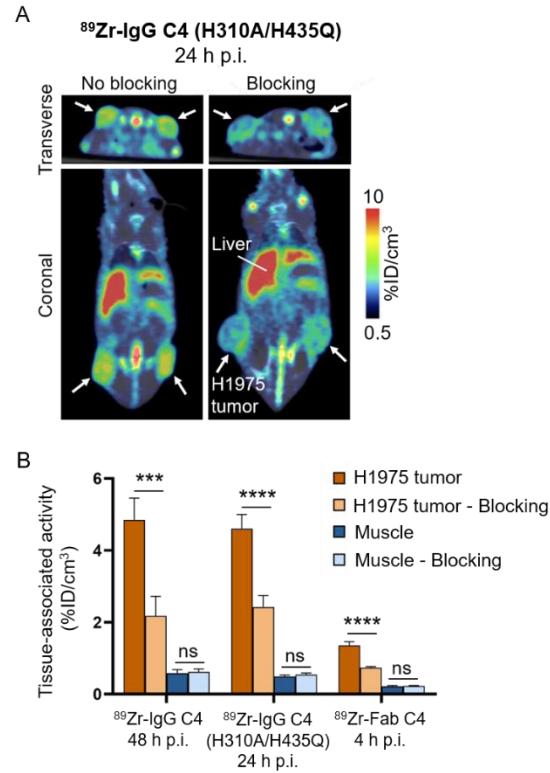


**Figure 3. PD-L1-specific tumor targeting of the C4 radioligands.** (A) Representative microPET/CT image sections of mice bearing PD-L1<sup>+</sup> H1975 xenografts (white arrows). (B) Image-derived C4 radioligand uptakes in H1975 tumor and muscle. Data are presented as mean  $\pm$  SD, N = 6 mice/group (no blocking), and N = 3-4 mice/group (blocking). A two-tailed unpaired Student t test was used for data comparison. ns: not significant, %ID/cm<sup>3</sup>: percentage injected dose per volume of tissue.

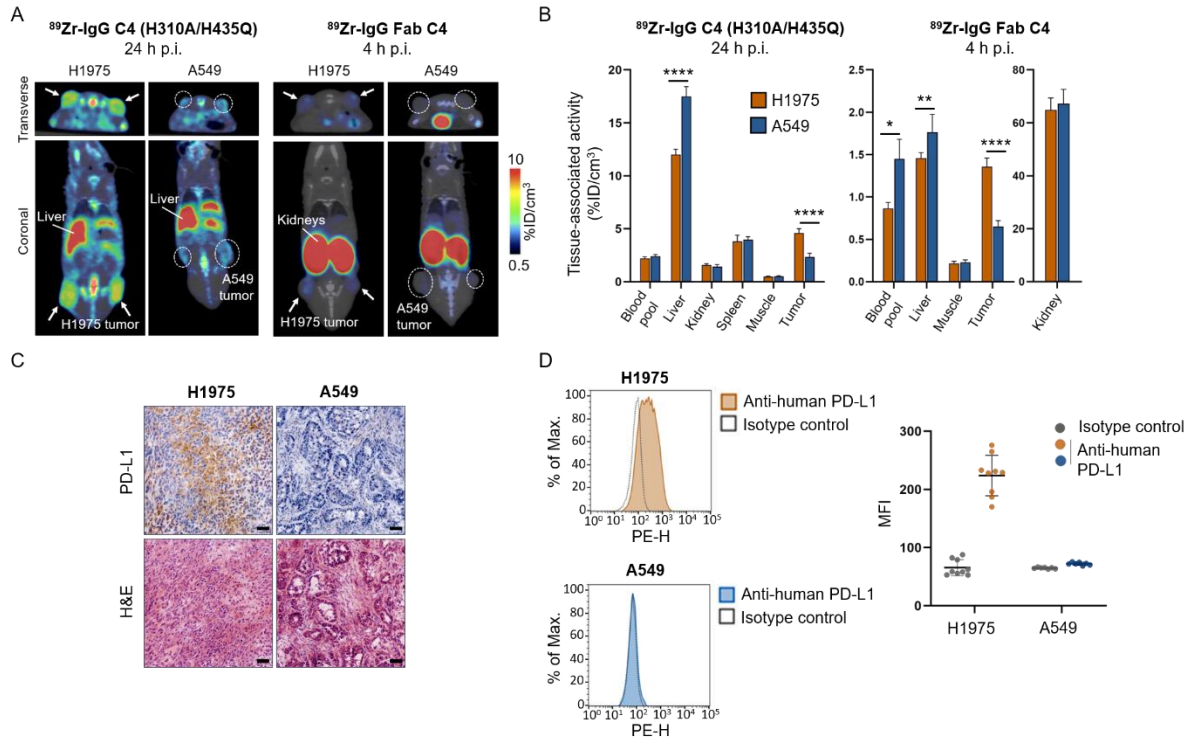


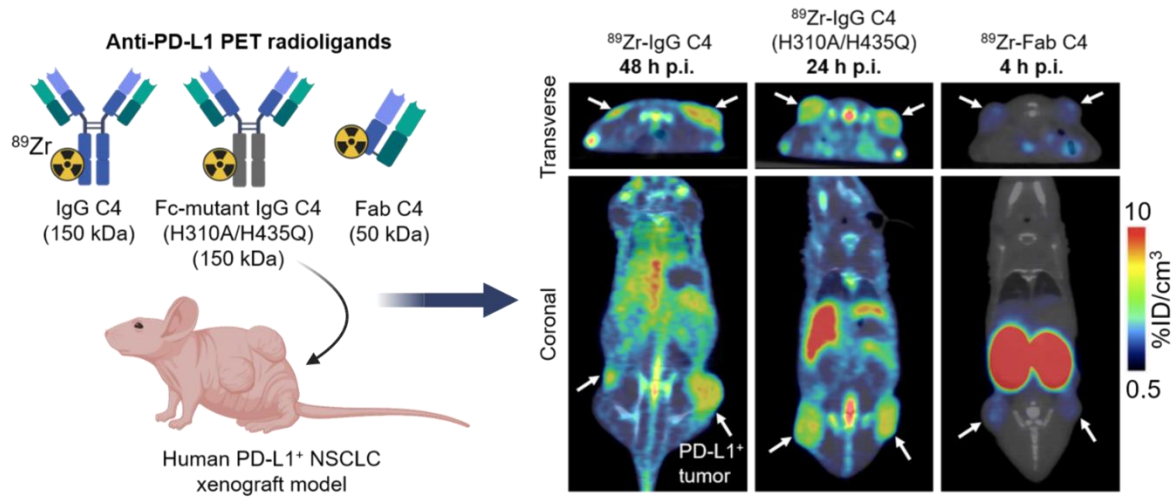
**Figure 4. microPET/CT imaging with the C4 radioligands in human NSCLC xenograft models with positive or negative PD-L1 expression.** (A) Representative microPET/CT image sections of mice bearing PD-L1<sup>+</sup> H1975 xenografts (white arrows) and PD-L1<sup>-</sup> A549 xenografts (dotted white circles). (B) Image-derived *in vivo* biodistribution of the C4 radioligands. Data are presented as mean  $\pm$  SD, N = 5-6 mice/group. A two-tailed unpaired Student t test was used for data comparison. (C) Representative images of tumor sections after PD-L1 IHC and hematoxylin and eosin (H&E) staining post-imaging. Scale bars: 50  $\mu\text{m}$ . (D) Representative flow cytometry histograms for cell-surface PD-L1 expression on tumor-derived single-cell suspensions. MFI values are shown on the dot plot (N = 9 H1975 tumors, N = 7 A549 tumors). MFI: median fluorescence intensity, %ID/cm<sup>3</sup>: percentage injected dose per volume of tissue.

**Table 1. Estimated blood PK parameters.**

	<sup>89</sup> Zr-IgG C4	<sup>89</sup> Zr-IgG C4 (H310A/H435Q)	<sup>89</sup> Zr-Fab C4
<b>t<sub>1/2β</sub> (h)</b>	80.25	86.55	1.50
<b>V<sub>c</sub> (mL)</b>	2.71	2.41	2.31
<b>CL (mL.h<sup>-1</sup>)</b>	0.047	0.16	2.46
<b>k<sub>10</sub> (h<sup>-1</sup>)</b>	0.017	0.066	1.06
<b>k<sub>12</sub> (h<sup>-1</sup>)</b>	0.11	0.08	1.91
<b>k<sub>21</sub> (h<sup>-1</sup>)</b>	0.12	0.02	1.92
<b>AUC<sub>plasma</sub> (%ID.h.mL<sup>-1</sup>)</b>	2137	629	41

AUC<sub>plasma</sub>: plasmatic exposure, CL: systemic clearance, k<sub>10</sub>: elimination rate constant from central compartment, k<sub>12</sub>: distribution rate constant from central to peripheral compartment, k<sub>21</sub>: distribution rate constant from peripheral to central compartment, t<sub>1/2β</sub>: biological elimination half-life, V<sub>c</sub>: volume of distribution of central compartment.

## Graphical Abstract



**Production of the C4 ligands.** The C4 IgG heavy and light chains were cloned into the AbVec2.0-IGHG1 and AbVec1.1-IGLC plasmids, respectively (16). For the Fab C4, the IgG Fc fragment was replaced by a polyhistidine (6xHIS) tag in the heavy chain plasmid. Human HEK293 Freestyle cells (Thermo-Fisher) ( $2.5 \times 10^6$  cells/mL) were transiently co-transfected in 100 mL of Freestyle medium (Thermo-Fisher), by adding 150  $\mu$ g of each recombinant plasmid and 1.8 mL of linear polyethylenimine (0.5 mg/mL, Polysciences). Transfected cells were incubated for 7 days at 37°C and 120 rpm, in a humidified atmosphere with 8% CO<sub>2</sub>. The culture supernatant containing the secreted C4 ligands was purified using HiTrap Protein A, Lambda FabSelect or HisTrap Excel columns (GE Healthcare) for IgG C4, IgG C4 (H310A/H435Q) and Fab C4, respectively. A final size-exclusion chromatography was performed using Sephacryl-S-200 HR columns (Sigma) with PBS. Purity of the C4 ligand solutions was evaluated by sodium dodecyl sulfate polyacrylamide gel electrophoresis (SDS-PAGE).

**Bio-layer interferometry.** Binding kinetics of the C4 ligands to human PD-L1 (Sinobiological) were determined by bio-layer interferometry, using an Octet RED96 instrument (ForteBio). Anti-hIgG Fc Capture Biosensors (ForteBio) were loaded with the IgG C4 or with the IgG C4 (H310A/H435Q) (50 nM) for 60 s. Association between the C4 IgGs and human PD-L1 was measured at different PD-L1 concentrations (1.6 nM-100 nM) for 300 s, before dissociation for 1000 s in kinetic buffer (PBS with 0.5% BSA and 0.05% Tween 20). Streptavidin Biosensors (ForteBio) were loaded with biotinylated human PD-L1 (50 nM) for 60 s. Association between the Fab C4 and human PD-L1 was measured at different Fab concentrations (0.78 nM-6.3 nM) for 200 s, before dissociation for 1000 s in kinetic buffer. After baseline subtraction, binding curves were fitted to a global 1:1 binding model to calculate the different kinetic constants ( $k_a$ ,  $k_d$ ,  $K_D$ ).

**Radiolabeling of the C4 ligands with <sup>89</sup>Zr.** The C4 ligands were covalently conjugated with the chelator p-isothiocyanatobenzylferrioxamine (p-NCS-Bz-DFO, Macrocyclics) on random lysine residues. Radiolabeling with <sup>89</sup>Zr (PerkinElmer) was performed according to a previously published protocol (17). 1 mL of C4 ligand solution (5 mg/mL in PBS) was adjusted to pH 9.3 with sodium carbonate (Na<sub>2</sub>CO<sub>3</sub>, 0.1 M). A 4-fold molar excess of p-NCS-Bz-DFO (10 mM in DMSO) was added dropwise to the C4 ligand solution with rigorous mixing (500 rpm). The reaction mixture was then gently mixed (350 rpm) for 45 min at 37°C. The DFO-C4 ligand conjugates were subsequently purified with a PD-10 column (GE Healthcare), using a gentisic acid solution (5 mg/mL in 0.25 M sodium acetate, pH 5.4-5.6) as the mobile phase. 200  $\mu$ L of [<sup>89</sup>Zr]Zr-oxalic acid solution (1 M) were neutralized with 90  $\mu$ L of Na<sub>2</sub>CO<sub>3</sub> (2 M). 500  $\mu$ L of DFO-C4 ligand solution (2.5 mg/mL) were then incubated with <sup>89</sup>Zr (111 MBq) for 1 h at 37°C. The reaction mixture was adjusted to pH 7.2 with HEPES (1 M, pH 7.1-7.3). The <sup>89</sup>Zr-labeled DFO-C4 ligand conjugates were first purified with a PD-10 column using a gentisic acid solution as the mobile phase, before being further concentrated and buffer exchanged in HEPES (0.5 M, pH 7.1-7.3) with a Vivaspin centrifugal concentrator (Sartorius). Radiochemical purity of the <sup>89</sup>Zr-DFO-C4 solution was assessed by instant thin layer chromatography (iTLC) and size-exclusion high-performance liquid chromatography (SE-HPLC). iTLC was performed on iTLC-SG glass microfiber papers impregnated with silica gel (Agilent Technologies) as the stationary phase, using a citric acid solution with 5% acetonitrile (20 mM, pH 4.9-5.1) as the mobile phase. The iTLC papers were read in a Mini-Scan TLC Imaging Scanner (Eckert & Ziegler). SE-HPLC was performed using a DIONEX System (Thermo-Fisher) with a bioZen 1.8  $\mu$ m SEC-2 LC column (Phenomenex). A linear-gradient elution was carried out with a solution of KH<sub>2</sub>PO<sub>4</sub> (50 mM) and KCl (250 mM) (pH 6.8), at a flow rate of 0.2 mL/min. Eluted species were detected with a UV detector (UVD 170U UV/VIS) and a scintillation detector (Packard).

**Cell culture.** The human NSCLC cell lines H1975 (ATCC CRL-5908) and A549 (ATCC CCL-185) were purchased from the American Type Culture Collection (ATCC). Cells were cultured in RPMI-1640 medium with GlutaMAX (Gibco) for the H1975 cell line or Dulbecco's Modified Eagle's medium with GlutaMAX (Gibco) for the A549 cell line, supplemented with 10% fetal bovine serum (Gibco) and 1% antibiotic-antimycotic solution (Gibco), at 37°C in a humidified atmosphere with 5% CO<sub>2</sub>. Cell lines were regularly tested negative for mycoplasma contamination with the MycoAlert Mycoplasma Detection Kit (Lonza). Low-passage (P20-P25) cell cultures were used for all experiments.

**Cell binding assays.** H1975 cells were harvested in their exponential phase of growth and resuspended in RPMI culture medium (Gibco) with 1% BSA (Thermo-Fisher) at a concentration of 8 million cells/mL. 250  $\mu$ L of cell solution (2 million cells) were mixed with 250  $\mu$ L of <sup>89</sup>Zr-IgG C4, <sup>89</sup>Zr-IgG C4 (H310A/H435Q) or <sup>89</sup>Zr-Fab C4 (2 pmol, 4-8  $\mu$ Ci) in HEPES buffer. For each C4 radioligand, a blocking experiment was also performed by mixing 250  $\mu$ L of cell solution

with 250  $\mu\text{L}$  of C4 radioligand (2 pmol) and 100X molar excess of non-radiolabeled C4 ligand in HEPES buffer. The reaction mixture was incubated for 2 h at 37°C. Cells were then washed 3 times with cold PBS and cell-associated activity was measured with the Wizard<sup>2</sup> gamma counter (PerkinElmer). Cell-associated activity was expressed as percentage of the total activity added per sample. Each condition was performed in N = 6 replicates.

**Immunoblotting.** PD-L1 expression in human NSCLC cell lines was evaluated by Western blot analysis. Total protein concentration in cell lysates was determined by a BCA protein assay kit (Sigma-Aldrich). Equal amounts (30  $\mu\text{g}$ ) of total proteins were separated by SDS-PAGE on 4-15% Mini-PROTEAN TGX gels (Bio-Rad) and transferred over to a polyvinylidene fluoride (PVDF) membrane by semi-dry blotting. After transfer, blots were blocked for 2 h at RT with 5% BSA (Thermo-Fisher) and incubated overnight at 4°C with the following primary antibodies: rabbit anti-human PD-L1 (1:1000, clone E1L3N, Cell Signaling #13684) and rabbit anti-human  $\alpha$ -tubulin (1:1000, Cell Signaling #2144). Blots were then incubated for 1 h at RT with an HRP-conjugated donkey anti-rabbit secondary antibody (1:10,000, Jackson ImmunoResearch 711-035-152). Proteins were detected using the Clarity Western ECL Substrate (Bio-Rad). Immunoblots were imaged with the FUSION FX imaging system (Vilber). Image post-processing (cropping, global contrast adjustment) was performed with ImageJ (v1.53i).

**Animals.** Female nude mice (*Mus musculus*, NMRI-FOXN1 Nu/Nu, Janvier, 10  $\pm$  1 weeks, 27.8  $\pm$  1.4 g) were used for the PET imaging studies. Animal experiments were performed according to the European Directive 2010/63/EU on the protection of laboratory animals and to its transposition into the French law (Decree No. 2013-118). The research project was conducted at the CEA-SHFJ imaging platform (authorization D91-471-105) and was approved by a local ethics committee (CETEA-CEA DSV IdF). Mice were housed in individually-ventilated cages in a temperature (22°C) and humidity (40%)-controlled room, with a 12-h light/12-h dark cycle. Animal experiments (subcutaneous injection of tumor cells, PET imaging) were performed under anesthesia with isoflurane in oxygen (3% for induction and 1.5–2% for maintenance) at 1.5 L.min<sup>-1</sup>. The body temperature of anesthetized mice was maintained at 37°C using heating pads.

**Subcutaneous injection of tumor cells.** Anesthetized mice were subcutaneously inoculated in both lower flanks with H1975 or A549 cells (4-5  $\times$  10<sup>6</sup> cells) suspended in PBS/Matrigel (BD Biosciences) (1:1). Subcutaneous tumor size and animal weight were measured two times per week. Mice were used for PET imaging studies when tumors reached  $\sim$ 8 mm at the largest diameter.

#### **microPET/CT imaging.**

**Radioligand injection.** Tumor-bearing mice received an intravenous bolus injection of <sup>89</sup>Zr-labeled C4 ligand in HEPES ( $\sim$ 100  $\mu\text{L}$ , 3.7  $\pm$  0.7 MBq, 7.0  $\pm$  3.0 MBq/nmol, 0.6  $\pm$  0.3 nmol) via a catheter placed in the lateral tail vein. For blocking studies, mice were co-injected with a 20X molar excess of non-radiolabeled C4 ligand ( $\sim$ 200  $\mu\text{L}$ , 1.2 nmol).

**PET/CT acquisition.** Whole-body PET emission scans were performed using an Inveon microPET scanner and an Inveon microPET/CT scanner (Siemens), with an axial field of view of 12.7 cm and a spatial resolution of  $\sim$ 1.5 mm full width half-maximum. A 350–650 keV energy window and a 3.43 ns timing window were used for data acquisition. A 60-min dynamic PET scan was performed immediately after injection of the C4 radioligand. 20-min static PET scans were subsequently acquired at selected times (4 h, 24 h, 48 h, 72 h and 7 days) post-injection (p.i.). For the Inveon microPET scanner, after each PET emission scan, a 6.6-min transmission scan using two rotating cobalt-57 (<sup>57</sup>Co) point sources (120-125 keV energy window) was recorded for photon attenuation correction. For the Inveon microPET/CT scanner, after each PET emission scan, a 11-min CT scan (120 projections, 220 total gantry rotations) was performed for photon attenuation correction and anatomical co-registration.

**PET/CT image reconstruction.** PET images were reconstructed with the Inveon Acquisition Workspace software (v2.1) using a three-dimensional ordinary Poisson ordered-subset expectation maximization followed by maximum *a posteriori* algorithm (OP-OSEM3D-MAP) (2 OSEM3D iterations, 18 MAP iterations with 16 MAP subsets). The size of the image matrix was 256 x 256 pixels with 159 slices, resulting in a voxel size of 0.38 x 0.38 x 0.80 mm. Normalization as well as corrections for dead-time, scatter, decay and attenuation were applied to all PET data. Dynamic PET images were arranged into 24 frames ranging from 0.5 to 5 min each (3 x 0.5 min, 5 x 1 min, 5 x 2 min, 3 x 3 min, 3 x 4 min, 4 x 5 min and 1 x 2.5 min). CT images were reconstructed using a Feldkamp cone beam reconstruction algorithm, with a cubic voxel size of 0.21 mm<sup>3</sup> in a 496 x 496 x 630 matrix.

**PET/CT image analysis.** Image analysis was performed with the PMOD software (v3.9). Volumes of interest (VOIs) were defined in main organs and tumor based on both CT (when available) and PET images. Fixed-size spherical VOIs (3.5-8 mm<sup>3</sup>) were drawn in representative parts of the heart, liver and kidneys. Mouse whole-body, spleen and subcutaneous tumors were delineated semi-automatically, with the help of the auto iso-contour tool. To quantify C4 radioligand uptake, the mean activity concentration (kBq/cm<sup>3</sup>) in each VOI was decay-corrected to the injection time and divided by the total injected activity (kBq) to obtain the percentage of injected dose per volume of tissue (%ID/cm<sup>3</sup>).

**Ex vivo biodistribution.** Immediately after the last PET imaging session, mice were sacrificed by cervical dislocation. Blood and major organs (brain, heart, lung, liver, kidney, spleen, intestine, tumor, muscle, bone) were collected, weighed, and counted with a Wizard<sup>2</sup> gamma counter (PerkinElmer). Radioactivity data (kBq) were background-corrected, decay-corrected to injection time and divided by the total injected activity (kBq) and the organ weight (g), to obtain the percentage injected dose per gram of tissue (%ID/g). Supplemental Figure 3.

**Immunohistochemistry.** PD-L1 expression in NSCLC xenografts was evaluated *ex vivo* by immunohistochemistry (IHC). Excised tumors were snap-frozen and stored at -80°C until processing. Frozen tumors were cryo-sectioned into 12-µm thick slices. Frozen tumor sections were fixed for 10 min at RT in 10% neutral-buffered formalin solution (Sigma-Aldrich). Non-specific binding sites were blocked by incubation for 2 h at RT with 10% FBS (Gibco) and 1% bovine serum albumin (BSA) (Thermo-Fisher). After blocking, slides were incubated overnight at 4°C with a rabbit anti-human PD-L1 primary antibody (1:100, clone E1L3N, Cell Signaling #13684). Slides were then rinsed and incubated for 1 h at RT with an HRP-conjugated donkey anti-rabbit secondary antibody (1:500, Jackson ImmunoResearch 711-035-152). Peroxidase activity was detected by incubating slides for 30 min at RT with 3-3'-diaminobenzidine (DAB) (BD Pharmingen). Tumor sections were subsequently counterstained with Harris hematoxylin (Sigma-Aldrich). Slides were eventually mounted with the Eukitt Quick-hardening mounting medium (Fluka Analytical). Standard hematoxylin and eosin (H&E) staining was also performed on adjacent tumor sections, using Harris hematoxylin and Eosin Y alcoholic (Sigma-Aldrich). Transmitted light images of stained tumor sections were acquired with the Axio Observer 5 microscope (Zeiss) at 20X magnification. Image post-processing (stitching, white balance, global contrast adjustment and addition of scale bar) was performed with the ZEN software (v2.6, Zeiss).

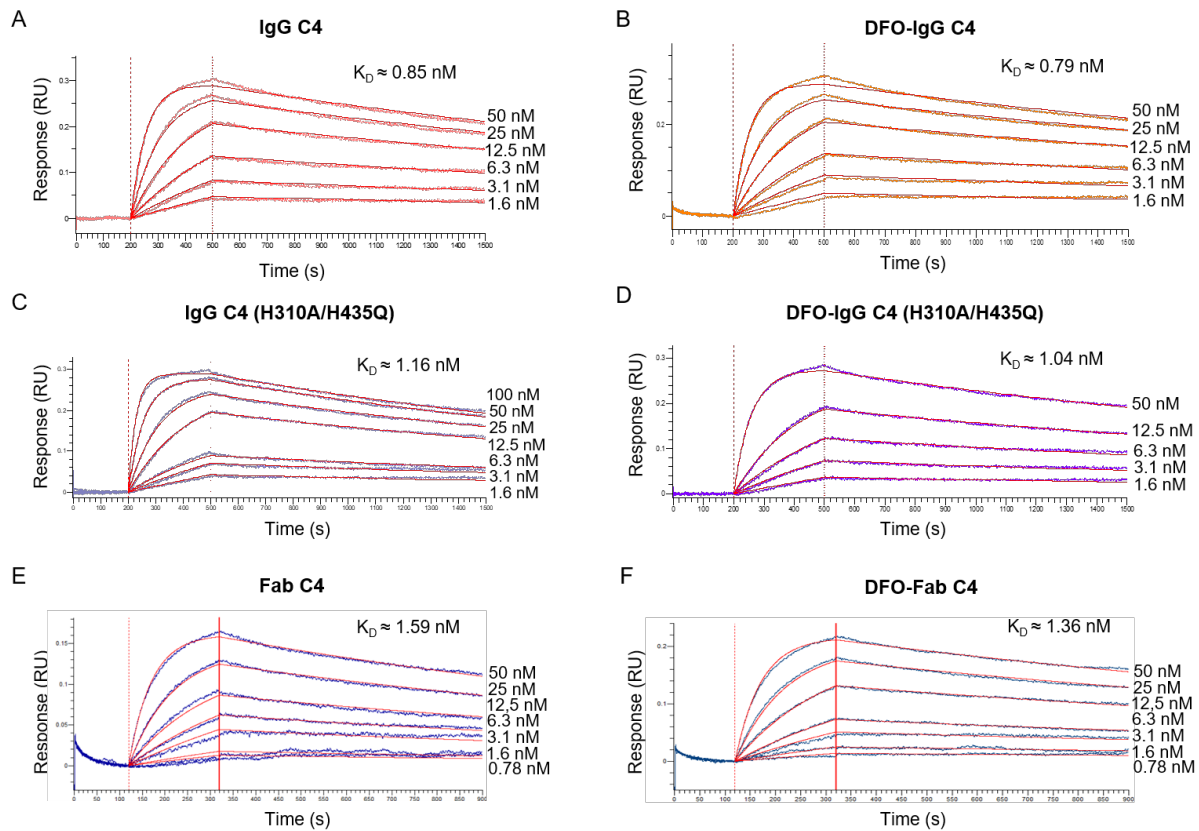
**Flow cytometry.** PD-L1 cell surface expression on human NSCLC cells cultured *in vitro* and on cell suspensions obtained from dissociated human NSCLC xenografts was evaluated by flow cytometry. Immediately after surgical excision, NSCLC tumors were minced into small tissue fragments and incubated in Accutase enzyme cocktail (Sigma-Aldrich) for 1 h at 37°C with regular mixing. Digested tumor tissues were filtered through cell strainers (PluriSelect) of decreasing mesh sizes (500, 200, 70 and 40 µm). Single-cell suspensions (~10<sup>6</sup> cells per sample) were incubated for 20 min on ice with the following fluorescent-labeled antibodies (100 µL, 10 µg/mL) in cell staining buffer (BioLegend): PE-conjugated anti-human PD-L1 antibody (clone 29E.2A3, BioLegend #329706) and PE-conjugated mouse IgG2b, κ isotype control (clone MPC-11, BioLegend #400314). For assessment of cell viability, cells were incubated for 30 min at RT with the Zombie Green viability dye (1:500, BioLegend). After incubation in fluorescent reagents, cells were washed 2 times and resuspended in cell staining buffer. Flow cytometry acquisitions were performed on the Attune NxT Acoustic Focusing Cytometer (Invitrogen). Unstained and single-color compensation controls were used for data compensation. Data analysis was performed with the FlowJo software (v10.7).

**Blood pharmacokinetics.** Plasma activity concentrations of the C4 radioligands were calculated from their image-derived blood pool activity concentrations. Considering that antibodies/antibody fragments do not partition into red blood cells and are restricted to the plasma, a blood-to-plasma concentration ratio of 0.55 was used. For each C4 radioligand, plasma time-activity curves (TACs) of individual mice were pooled together and fitted to a two-compartment model with intravenous bolus input and first-order elimination, using the NONMEM software (v6.2).

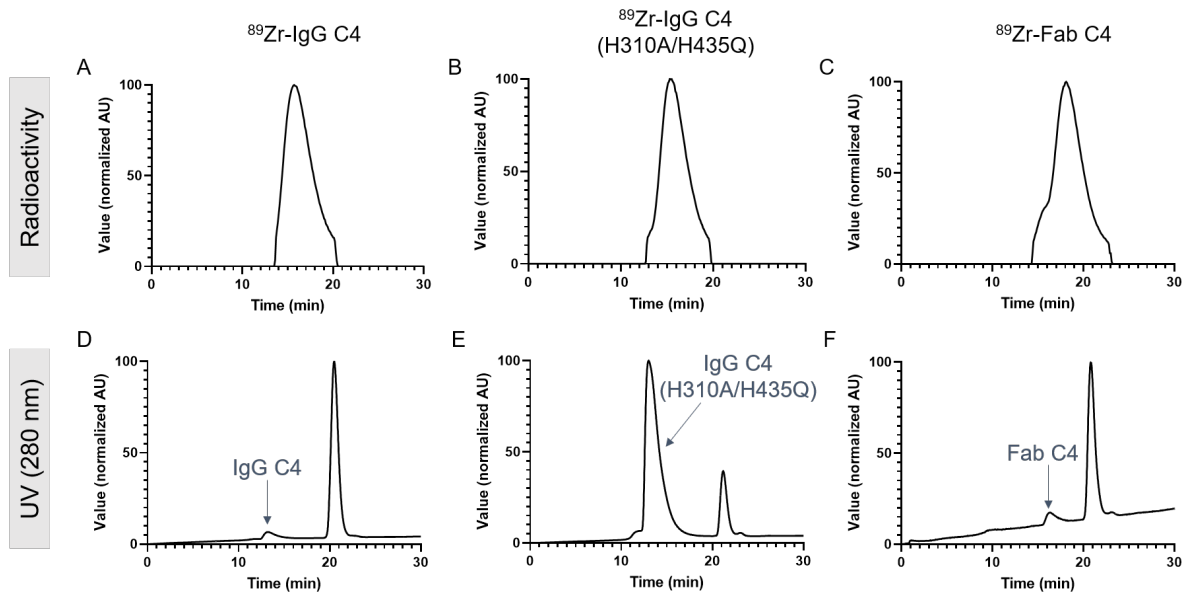
**Dosimetry analysis.** For each C4 radioligand, human organ absorbed dose estimates were extrapolated from longitudinal biodistribution data in mice. For each mouse, non-decay-corrected mean activity concentrations (Bq/cm<sup>3</sup>) in main source organs (blood pool, liver, kidneys, spleen, whole-body) were derived from PET images and multiplied by corresponding organ volumes to obtain the organ mean activities (Bq). Organ mean activities were

plotted against time to obtain the organ TACs. Each organ TAC was numerically integrated (trapezoidal method) over the imaging time-course, and a single exponential decay function with the half-life of  $^{89}\text{Zr}$  was extrapolated and analytically integrated beyond the last imaging time point with the R software (v4.0.4). The organ cumulated activity (Bq/s) was derived as the sum of the numerical and analytical integrations. For each mouse, source organ cumulated activities (Bq/s) were divided by the total administered activity (Bq) to obtain the organ residence times (kBq.h/kBq). The cumulated activity in the remainder of the body was calculated as the difference between the whole-body cumulated activity and the cumulated activities in all other source organs. Murine source organ residence times were used as input in the IDAC-Dose (v2.1) software (18) for calculation of human organ absorbed doses and whole-body effective dose. For the three C4 radioligands, murine organ absorbed doses were also estimated with the Rodent Dose Evaluation Software (RODES) (19).

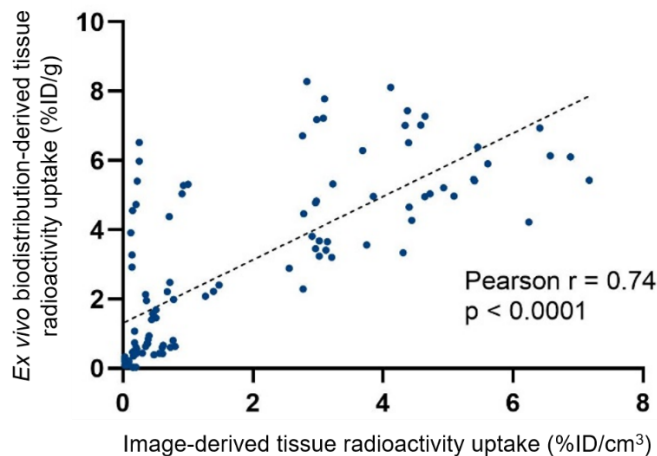
**Statistical analysis.** Statistical analyses were performed with GraphPad Prism (v9.0.1). Unless stated otherwise, data are presented as mean  $\pm$  standard deviation (SD). Two-tailed unpaired or paired Student t tests were used for two-group data comparison (\*  $P < 0.05$ , \*\*  $P < 0.01$ , \*\*\*  $P < 0.001$ , \*\*\*\*  $P < 0.0001$ ).



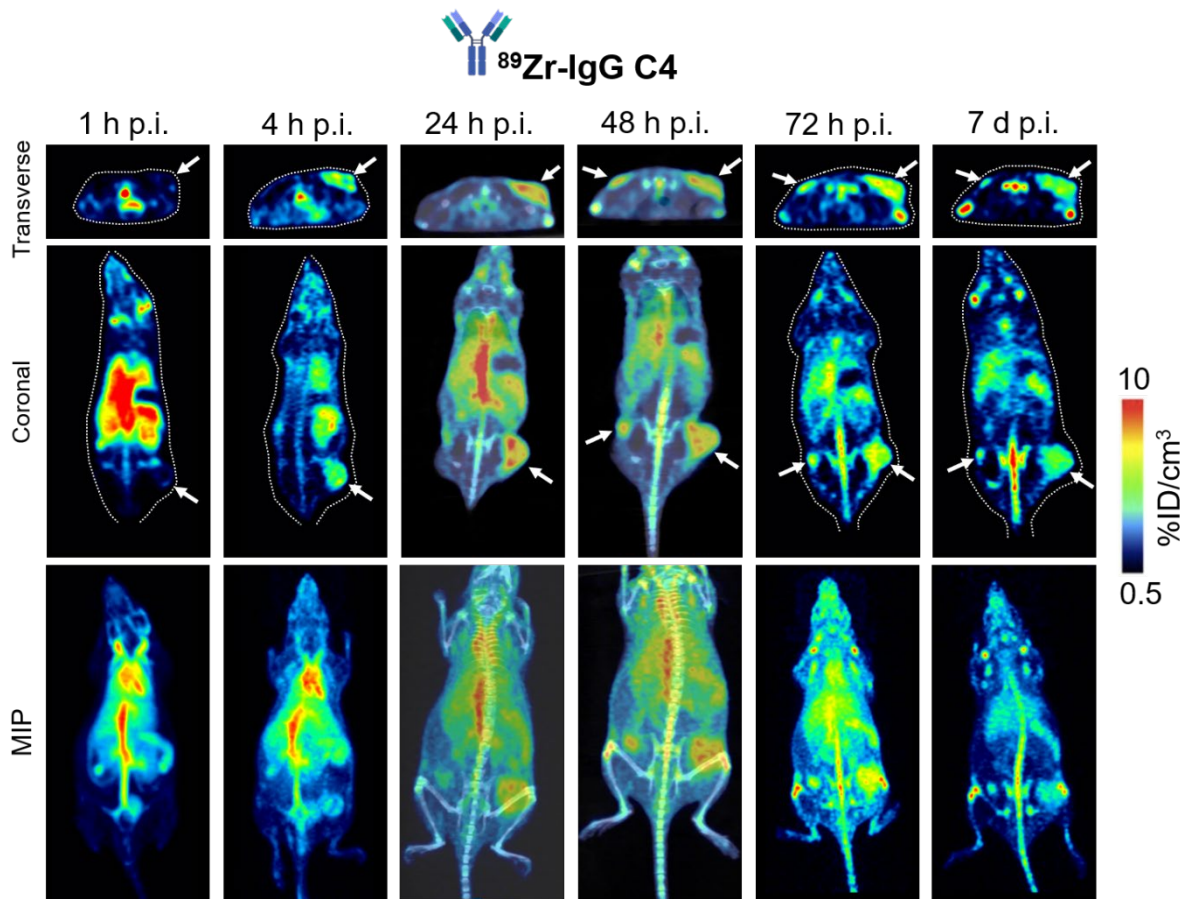
**Supplemental Figure 1. Binding kinetics of the C4 ligands to human PD-L1.** Bio-layer interferometry sensorgrams of binding of IgG C4 (A), DFO-IgG C4 (B), IgG C4 (H310A/H435Q) (C), DFO-IgG C4 (H310A/H435Q) (D), Fab C4 (E) and DFO-Fab C4 (F) to the human PD-L1 protein. Affinity constant ( $K_D$ ) values are indicated. RU: response unit.



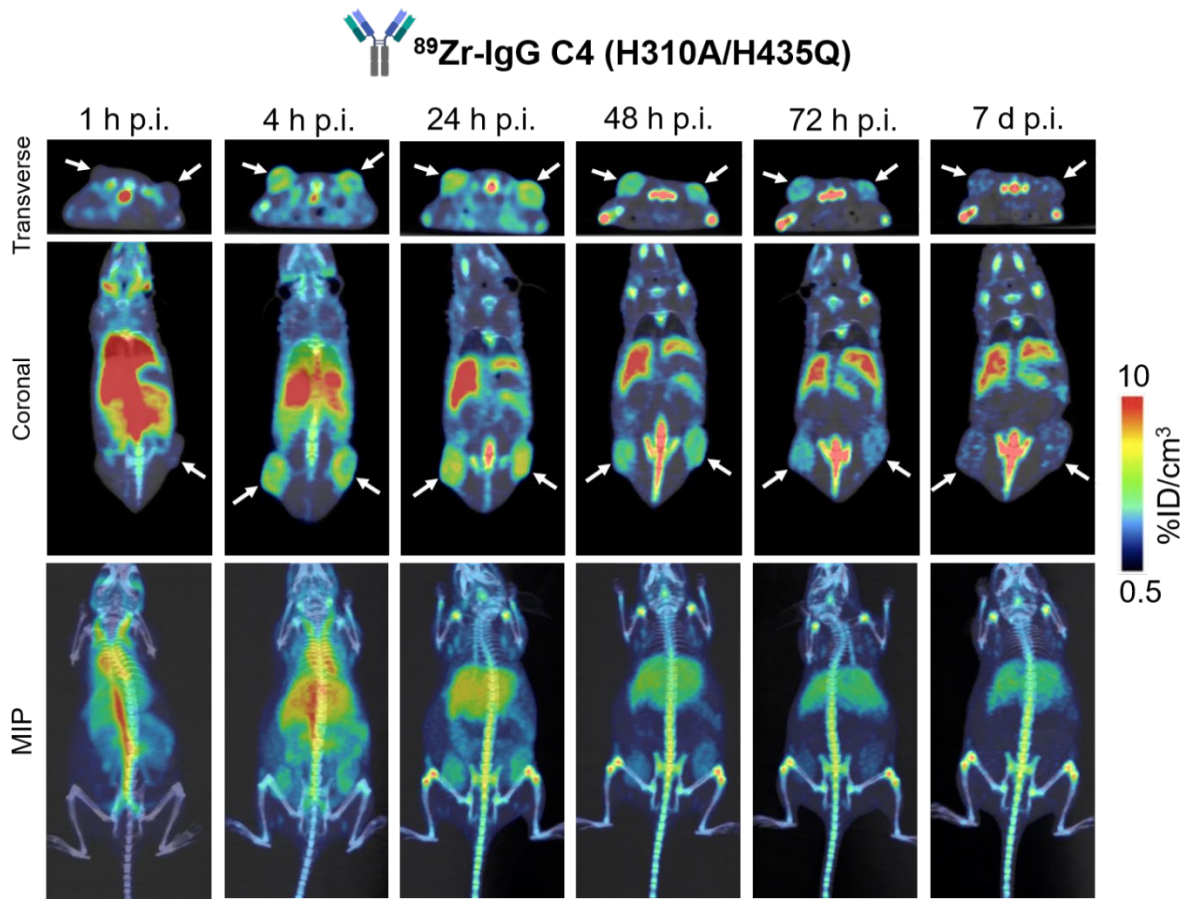
**Supplemental Figure 2. Assessment of radiochemical purity by HPLC after radiolabeling of the C4 ligands with  $^{89}\text{Zr}$ .** Representative HPLC chromatograms of purified  $^{89}\text{Zr}$ -IgG C4 (A and D),  $^{89}\text{Zr}$ -IgG C4 (H310A/H435Q) (B and E) and  $^{89}\text{Zr}$ -Fab C4 (C and F), with radioactivity detection (A, B and C) and UV detection at 280 nm (D, E, and F). The second peak observed at ~22 min on the UV chromatograms corresponds to the gentisic acid still remaining in the purified C4 radioligand solutions. AU: arbitrary unit, UV: ultraviolet.



**Supplemental Figure 3. Correlation between quantification of C4 radioligand tissue uptake by *ex vivo* biodistribution and by PET image analysis.** Tissue uptake values of the C4 radioligands derived from *ex vivo* biodistribution (heart, liver, kidneys, spleen, muscle and tumor) strongly correlated with those derived from analysis of PET images at the last imaging time-point (Pearson  $r = 0.74$ ,  $p < 0.0001$ ). Data from PET imaging experiments on H1975 tumor-bearing mice with the  $^{89}\text{Zr}$ -labeled IgG C4, IgG C4 (H310A/H435Q) and Fab C4, with or without blocking, were pooled ( $N = 6$  experiments). For the  $^{89}\text{Zr}$ -Fab C4, kidneys were excluded from the analysis as the *ex vivo* kidney counting gave values superior to 200 %ID/g. %ID/cm<sup>3</sup>: percentage injected dose per volume of tissue, %ID/g : percentage injected dose per gram of tissue.

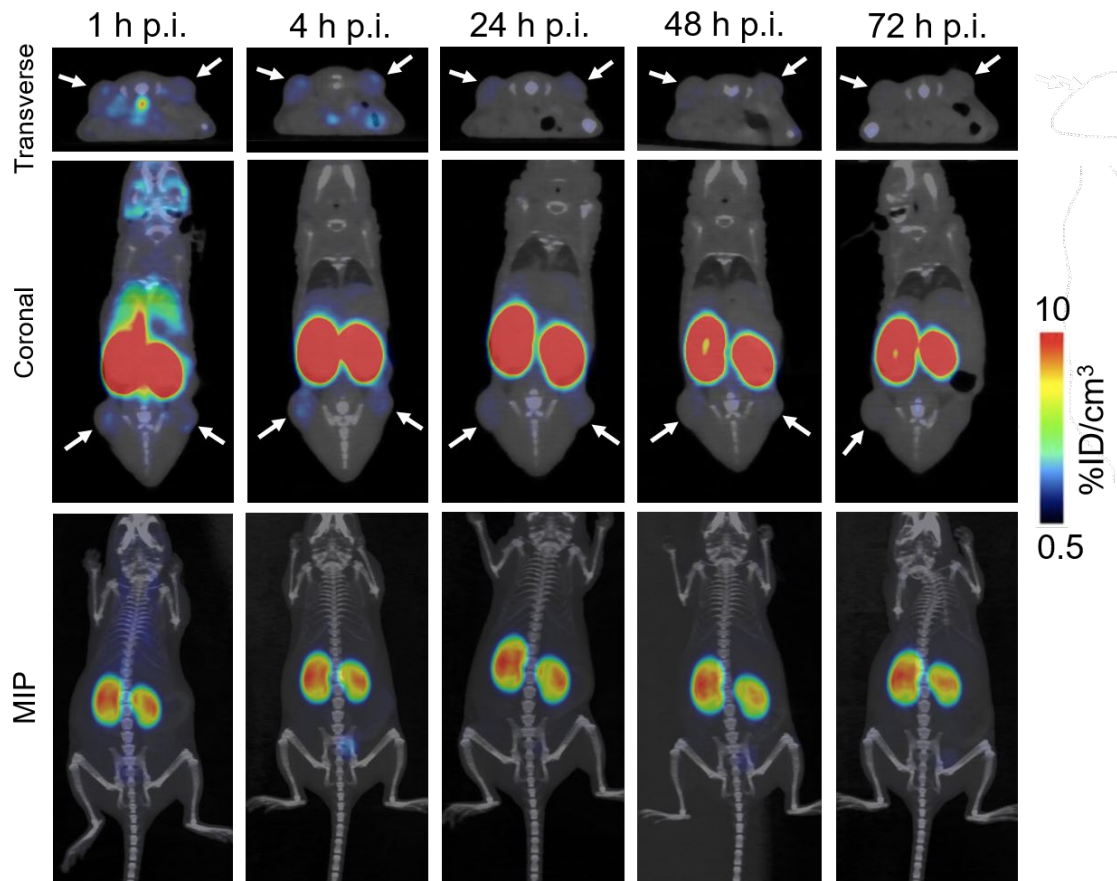


**Supplemental Figure 4. Longitudinal microPET/CT imaging with the anti-PD-L1 <sup>89</sup>Zr-IgG C4 in a PD-L1<sup>+</sup> human NSCLC xenograft model.** Representative microPET/CT image sections (transverse and coronal) and MIP images of female nude mice bearing subcutaneous PD-L1<sup>+</sup> H1975 xenografts (white arrows), obtained at selected times after <sup>89</sup>Zr-IgG C4 administration. MIP: maximum intensity projection, p.i.: post-injection, %ID/cm<sup>3</sup>: percentage injected dose per volume of tissue.

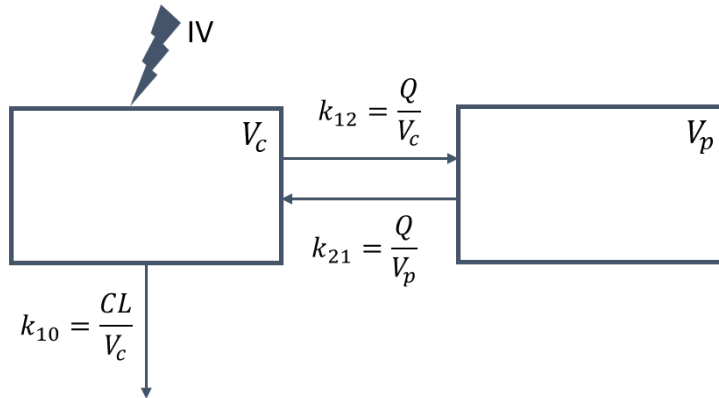


**Supplemental Figure 5. Longitudinal microPET/CT imaging with the anti-PD-L1 <sup>89</sup>Zr-IgG C4 (H310A/H435Q) in a PD-L1<sup>+</sup> human NSCLC xenograft model.** Representative microPET/CT image sections (transverse and coronal) and MIP images of female nude mice bearing subcutaneous PD-L1<sup>+</sup> H1975 xenografts (white arrows), obtained at selected times after <sup>89</sup>Zr-IgG C4 (H310A/H435Q) administration. MIP: maximum intensity projection, p.i.: post-injection, %ID/cm<sup>3</sup>: percentage injected dose per volume of tissue.

## <sup>89</sup>Zr-Fab C4

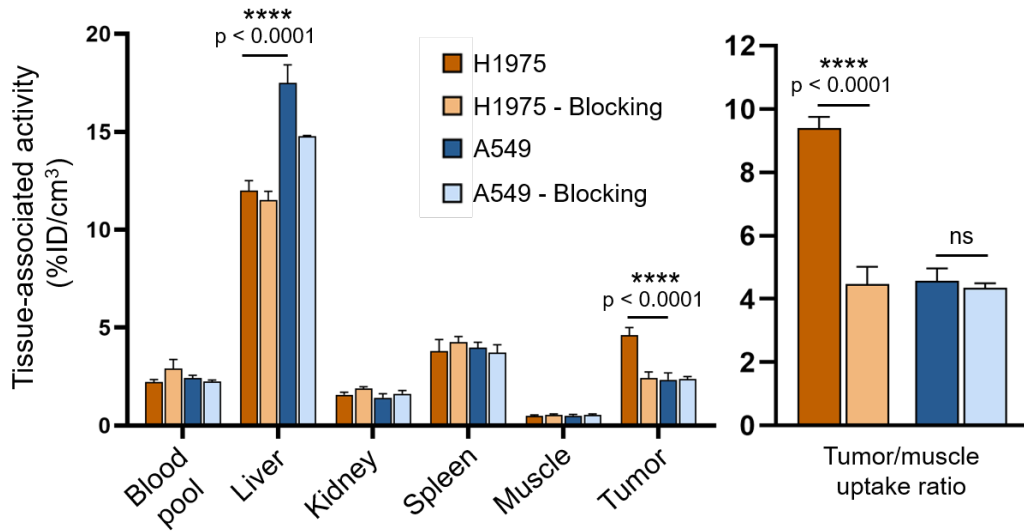


**Supplemental Figure 6. Longitudinal microPET/CT imaging with the anti-PD-L1 <sup>89</sup>Zr-Fab C4 in a PD-L1<sup>+</sup> human NSCLC xenograft model.** Representative microPET/CT image sections (transverse and coronal) and MIP images of female nude mice bearing subcutaneous PD-L1<sup>+</sup> H1975 xenografts (white arrows), obtained at selected times after <sup>89</sup>Zr-Fab C4 administration. MIP: maximum intensity projection, p.i.: post-injection, %ID/cm<sup>3</sup>: percentage injected dose per volume of tissue.

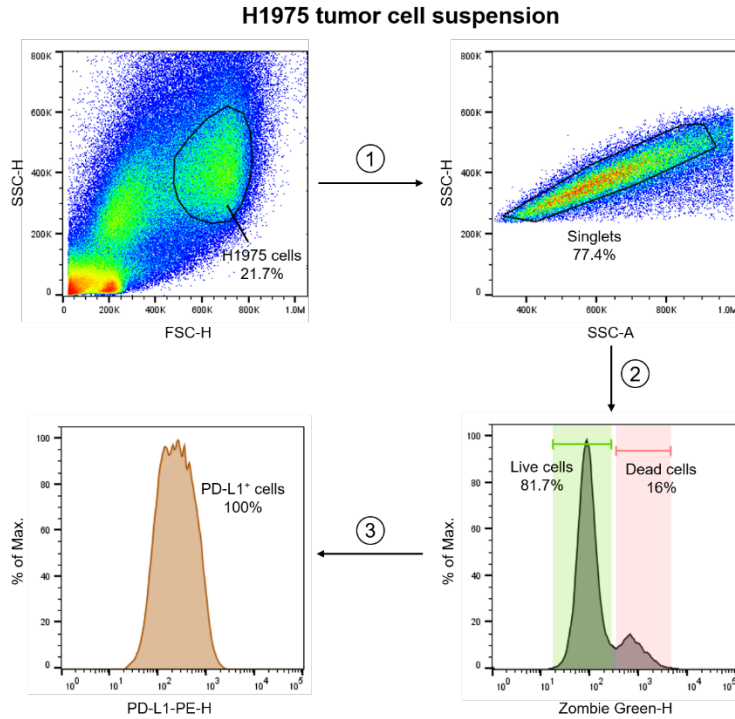


**Supplemental Figure 7. Schematic representation of a two-compartment model with intravenous bolus input and first-order elimination.** This model was used to fit the plasma time-activity curves of H1975 tumor-bearing female nude mice injected with the C4 radioligands. CL: clearance from central compartment, IV: intravenous injection,  $k_{10}$ : elimination rate constant from central compartment,  $k_{12}$ : distribution rate constant from central to peripheral compartment,  $k_{21}$ : distribution rate constant from peripheral to central compartment, Q: clearance from peripheral to central compartment,  $V_c$ : volume of distribution of central compartment,  $V_p$ : volume of distribution of peripheral compartment.

**<sup>89</sup>Zr-IgG C4 (H310A/H435Q)**  
24 h p.i.



**Supplemental Figure 8. PD-L1-specific tumor targeting of the <sup>89</sup>Zr-IgG C4 (H310A/H435Q).** Image-derived *in vivo* biodistribution of the <sup>89</sup>Zr-IgG C4 (H310A/H435Q) in female nude mice bearing subcutaneous PD-L1<sup>+</sup> H1975 xenografts or PD-L1<sup>-</sup> A549 xenografts. For blocking experiments, mice were co-injected with a 20X molar excess of non-radiolabeled IgG C4 (H310A/H435Q). While this blocking dose significantly reduced <sup>89</sup>Zr-IgG C4 (H310A/H435Q) uptake in H1975 xenografts (by ~50%), it did not affect radioligand uptake in A549 xenografts. <sup>89</sup>Zr-IgG C4 (H310A/H435Q) uptake in non-blocked and blocked A549 tumors were similar to that in blocked H1975 tumors (~2-2.5 %ID/cm<sup>3</sup>). Data are presented as mean ± SD, N = 6 mice/group (no blocking) and N = 3-4 mice/group (blocking). A two-tailed unpaired Student t test was used for two-group data comparison. p.i.: post-injection, %ID/cm<sup>3</sup>: percentage injected dose per volume of tissue.



**Supplemental Figure 9. Gating strategy employed for flow cytometry experiments on single-cell suspensions derived from solid tumors.** Representative plots obtained in a flow cytometry experiment on H1975 tumor cells incubated with the Zombie Green viability dye and a PE-conjugated anti-human PD-L1 antibody. (1) Cells were first gated based on forward scatter (FSC) and side scatter (SSC) characteristics on the SSC-H vs FSC-H density plot. (2) Coincident events that could represent cell clumps were excluded by gating singlets on the SSC-H vs SSC-A density plot. (3) Viable cells were then selected on the Zombie Green-H histogram: the first peak (Zombie Green negative) represented the fraction of viable cells within the sample, whereas the second peak (Zombie Green positive) represented dead cells with compromised membranes permeant to the fluorescent dye. No further gating was performed. For each gate, the percentage of events from the parent gate is indicated. PE: phycoerythrin.

**Supplemental Table 1. Murine dosimetry of the C4 radioligands.** For each C4 radioligand, cumulated activities (Bq/s) in main source organs (blood pool, liver, kidneys, spleen) of individual mice were used as input in the RODES software for calculation of murine organ absorbed doses (mGy). The RODES female mouse phantom (20 g) was selected. For each mouse, estimated absorbed doses were divided by the total administered activity (MBq). Data are presented as mean  $\pm$  SD. Organs with the highest absorbed dose estimates are indicated in bold.

Target organ	Organ absorbed dose estimate (mGy/MBq)		
	<sup>89</sup> Zr-IgG C4 N = 5 mice	<sup>89</sup> Zr-IgG C4 (H310A/H435Q) N = 6 mice	<sup>89</sup> Zr-Fab C4 N = 6 mice
<b>Heart</b>	<b>1.13 <math>\pm</math> 0.10</b>	<b>1.22 <math>\pm</math> 0.04</b>	<b>0.34 <math>\pm</math> 0.07</b>
Lungs	0.18 $\pm$ 0.01	0.25 $\pm$ 0.01	0.06 $\pm$ 0.02
<b>Liver</b>	<b>0.41 <math>\pm</math> 0.01</b>	<b>0.73 <math>\pm</math> 0.04</b>	<b>0.12 <math>\pm</math> 0.01</b>
Stomach	0.05 $\pm$ 0.001	0.08 $\pm$ 0.004	0.05 $\pm$ 0.01
<b>Spleen</b>	<b>0.24 <math>\pm</math> 0.02</b>	0.18 $\pm$ 0.01	0.10 $\pm$ 0.02
<b>Kidneys</b>	0.22 $\pm$ 0.02	<b>0.37 <math>\pm</math> 0.03</b>	<b>1.97 <math>\pm</math> 0.29</b>
Esophagus	0.16 $\pm$ 0.002	0.26 $\pm$ 0.013	0.05 $\pm$ 0.007
Intestines	0.01 $\pm$ 0.001	0.02 $\pm$ 0.001	0.02 $\pm$ 0.004
Colon	0.018 $\pm$ 0.0004	0.03 $\pm$ 0.002	0.05 $\pm$ 0.008
Spinal cord	0.01 $\pm$ 0.0004	0.02 $\pm$ 0.001	0.02 $\pm$ 0.002
Skeleton	0.01 $\pm$ 0.0003	0.02 $\pm$ 0.001	0.01 $\pm$ 0.001
Thyroid	0.004 $\pm$ 0.0002	0.01 $\pm$ 0.0003	0.003 $\pm$ 0.0003
Ovaries	0.01 $\pm$ 0.001	0.03 $\pm$ 0.001	0.09 $\pm$ 0.01
Soft tissues	0.02 $\pm$ 0.001	0.03 $\pm$ 0.002	0.03 $\pm$ 0.003
Whole-body	0.06 $\pm$ 0.001	0.09 $\pm$ 0.004	0.07 $\pm$ 0.01

**Supplemental Table 2. Binding kinetics of the C4 ligands to human PD-L1.** Kinetic constants of C4 ligand binding to human PD-L1 were measured by bio-layer interferometry.

C4 ligand	K <sub>D</sub> (nM)	k <sub>a</sub> (M <sup>-1</sup> .s <sup>-1</sup> )	k <sub>d</sub> (s <sup>-1</sup> )
IgG C4	0.85	3.67 x 10 <sup>5</sup>	3.15 x 10 <sup>-4</sup>
DFO-IgG C4	0.79	3.76 x 10 <sup>5</sup>	2.99 x 10 <sup>-4</sup>
IgG C4 (H310A/H435Q)	1.16	3.47 x 10 <sup>5</sup>	4.04 x 10 <sup>-4</sup>
DFO-IgG C4 (H310A/H435Q)	1.04	3.39 x 10 <sup>5</sup>	3.53 x 10 <sup>-4</sup>
Fab C4	1.59	3.95 x 10 <sup>5</sup>	6.31 x 10 <sup>-4</sup>
DFO-Fab C4	1.36	3.86 x 10 <sup>5</sup>	5.27 x 10 <sup>-4</sup>

**Supplemental Table 3. Quality control of radiochemical purity after radiolabeling of the C4 ligands with <sup>89</sup>Zr. N = 2 experiments per C4 radioligand.**

	<sup>89</sup> Zr-IgG C4	<sup>89</sup> Zr-IgG C4 (H310A/H435Q)	<sup>89</sup> Zr-Fab C4
Radiochemical purity assessed by HPLC (%)	>96	>98	>96
Radiochemical purity assessed by iTLC (%)	>97	>95	>95

**Supplemental Table 4. Summary of the PET/CT imaging experiments performed in the human NSCLC xenograft models (H1975 and A549) with the anti-PD-L1 C4 radioligands.** For each experiment, activities were decay-corrected to the injection time. Data are presented as mean ± SD.

NSCLC tumor model	<sup>89</sup> Zr-labeled C4 ligand	Specific activity (MBq/nmol)	Injected activity (MBq)	Injected quantity (nmol)	Co-injected cold C4 ligand quantity (nmol)	Number of mice
H1975	IgG C4	11.6	4.3 ± 0.4	0.36 ± 0.03	/	6
	IgG C4	9.5	3.7 ± 0.4	0.40 ± 0.04	1.2 nmol	3
	IgG C4 (H310A/H435Q)	6.2	4.2 ± 0.2	0.66 ± 0.03	/	6
	IgG C4 (H310A/H435Q)	6.2	3.7 ± 0.2	0.60 ± 0.02	1.2 nmol	4
	Fab C4	7.5	4.0 ± 0.3	0.54 ± 0.03	/	6
	Fab C4	7.5	4.2 ± 0.3	0.57 ± 0.03	1.2 nmol	4
A549	IgG C4 (H310A/H435Q)	5.3	2.4 ± 0.2	0.45 ± 0.03	/	6
	Fab C4	2.0	2.6 ± 0.3	1.33 ± 0.13	/	5

**Supplemental Table 5. Biodistribution of the C4 radioligands in a PD-L1<sup>+</sup> human NSCLC xenograft model.** Female nude mice bearing subcutaneous PD-L1<sup>+</sup> H1975 xenografts were injected with the C4 radioligands, and PET/CT scans were acquired at selected times post-injection. Image-derived radioligand tissue uptake was expressed as percentage of injected dose per volume of tissue (%ID/cm<sup>3</sup>). Data are presented as mean ± SD.

<b><sup>89</sup>Zr-IgG C4 uptake (%ID/cm<sup>3</sup>)</b>						
<b>N = 6 mice</b>						
<b>Time post-injection</b>	<b>1 h</b>	<b>4 h</b>	<b>24 h</b>	<b>48 h</b>	<b>72 h</b>	<b>7 d</b>
Blood pool	18.10 ± 7.53	12.33 ± 1.24	7.97 ± 3.29	5.95 ± 2.48	5.43 ± 2.24	2.85 ± 1.48
Liver	12.66 ± 5.23	8.85 ± 0.45	6.20 ± 0.28	6.18 ± 0.35	5.78 ± 0.38	5.12 ± 0.36
Kidney	8.03 ± 3.32	5.83 ± 0.17	3.71 ± 0.53	2.96 ± 0.46	2.99 ± 1.24	1.71 ± 0.96
Spleen	8.17 ± 3.38	7.35 ± 0.18	5.48 ± 0.43	4.83 ± 0.27	4.60 ± 0.15	4.41 ± 0.19
H1975 tumor	1.36 ± 0.60	4.06 ± 0.47	4.53 ± 0.32	4.85 ± 0.61	4.15 ± 0.50	3.78 ± 0.24
Muscle	0.80 ± 0.35	1.02 ± 0.05	0.72 ± 0.08	0.59 ± 0.10	0.62 ± 0.09	0.58 ± 0.06
<b><sup>89</sup>Zr-IgG C4 (H310A/H435Q) uptake (%ID/cm<sup>3</sup>)</b>						
<b>N = 6 mice</b>						
<b>Time post-injection</b>	<b>1 h</b>	<b>4 h</b>	<b>24 h</b>	<b>48 h</b>	<b>72 h</b>	<b>7 d</b>
Blood pool	20.70 ± 0.90	12.19 ± 0.66	2.22 ± 1.22	0.96 ± 0.53	0.71 ± 0.39	0.58 ± 0.33
Liver	11.84 ± 1.06	12.39 ± 0.61	12.00 ± 0.51	10.55 ± 0.38	10.66 ± 0.63	10.26 ± 0.44
Kidney	9.05 ± 0.21	5.49 ± 0.44	1.56 ± 0.86	1.05 ± 0.58	0.85 ± 0.47	0.64 ± 0.35
Spleen	7.35 ± 0.78	6.72 ± 0.49	3.81 ± 0.58	3.09 ± 0.49	3.24 ± 1.77	2.78 ± 1.53
H1975 tumor	1.48 ± 0.15	3.92 ± 0.51	4.60 ± 0.39	3.48 ± 0.33	2.69 ± 0.27	1.69 ± 0.89
Muscle	0.72 ± 0.06	0.79 ± 0.06	0.49 ± 0.05	0.43 ± 0.06	0.39 ± 0.03	0.31 ± 0.16
<b><sup>89</sup>Zr-Fab C4 uptake (%ID/cm<sup>3</sup>)</b>						
<b>N = 6 mice</b>						
<b>Time post-injection</b>	<b>1 h</b>	<b>4 h</b>	<b>24 h</b>	<b>48 h</b>	<b>72 h</b>	
Blood pool	6.48 ± 2.74	0.86 ± 0.48	0.19 ± 0.11	0.12 ± 0.07	0.11 ± 0.06	
Liver	2.90 ± 0.31	1.46 ± 0.07	1.02 ± 0.13	0.90 ± 0.41	0.83 ± 0.38	
Kidney	69.57 ± 28.48	64.91 ± 4.50	40.08 ± 0.99	29.58 ± 13.40	22.76 ± 10.20	
H1975 tumor	1.06 ± 0.12	1.36 ± 0.11	0.79 ± 0.12	0.59 ± 0.26	0.50 ± 0.23	
Muscle	0.54 ± 0.08	0.22 ± 0.02	0.14 ± 0.02	0.13 ± 0.06	0.12 ± 0.05	

**Supplemental Table 6. Blocking experiments.** Female nude mice bearing subcutaneous PD-L1<sup>+</sup> H1975 xenografts were injected with the C4 radioligands, with or without co-injection of a 20X molar excess of non-radiolabeled C4 ligand. PET/CT scans were acquired at the optimal imaging time point for each C4 radioligand. Image-derived radioligand tissue uptake was expressed as percentage of injected dose per volume of tissue (%ID/cm<sup>3</sup>). Data are presented as mean ± SD.

	Radioligand uptake (%ID/cm <sup>3</sup> )					
	<sup>89</sup> Zr-IgG C4 48 h p.i.		<sup>89</sup> Zr-IgG C4 (H310A/H435Q) 24 h p.i.		<sup>89</sup> Zr-Fab C4 4 h p.i.	
	No blocking N = 6 mice	Blocking N = 3 mice	No blocking N = 6 mice	Blocking N = 4 mice	No blocking N = 6 mice	Blocking N = 4 mice
Blood pool	5.95 ± 2.48	6.20 ± 0.51	2.22 ± 1.22	2.90 ± 1.70	0.86 ± 0.48	0.75 ± 0.43
Liver	6.18 ± 0.35	6.76 ± 0.48	12.00 ± 0.51	11.51 ± 0.44	1.46 ± 0.07	1.40 ± 0.07
Kidney	2.96 ± 0.46	3.04 ± 0.23	1.56 ± 0.86	1.89 ± 1.09	64.91 ± 4.50	61.07 ± 1.96
Spleen	4.83 ± 0.27	4.55 ± 0.33	3.81 ± 0.58	4.25 ± 2.46	/	/
H1975 tumor	4.85 ± 0.61	2.17 ± 0.55	4.60 ± 0.39	2.43 ± 0.32	1.36 ± 0.11	0.73 ± 0.03
Muscle	0.59 ± 0.10	0.61 ± 0.09	0.49 ± 0.05	0.54 ± 0.05	0.22 ± 0.02	0.22 ± 0.02

**Supplemental Table 7. Human dosimetry of the C4 radioligands.** For each C4 radioligand, residence times (kBq.h.kBq<sup>-1</sup>) in main source organs (blood pool, liver, kidneys, spleen, remainder of the body) of individual mice were used as input in the IDAC-Dose software for extrapolation of human organ absorbed doses (mGy/MBq) and effective dose (mSv/MBq). Data are presented as mean ± SD. Organs with the highest absorbed dose estimates are indicated in bold.

Organ	Organ absorbed dose estimate (mGy/MBq)		
	<sup>89</sup> Zr-IgG C4	<sup>89</sup> Zr-IgG C4 (H310A/H435Q)	<sup>89</sup> Zr-Fab C4
<b>Adrenals</b>	0.61 ± 0.08	0.82 ± 0.12	<b>1.34 ± 0.26</b>
Brain	0.17 ± 0.03	0.10 ± 0.02	0.07 ± 0.03
Breast	0.25 ± 0.03	0.24 ± 0.02	0.12 ± 0.02
Colon wall	0.25 ± 0.03	0.21 ± 0.03	0.24 ± 0.05
Endosteum (bone surface)	0.22 ± 0.03	0.16 ± 0.03	0.12 ± 0.04
<b>Gallbladder wall</b>	<b>0.74 ± 0.06</b>	<b>1.14 ± 0.09</b>	0.59 ± 0.19
<b>Heart wall</b>	<b>1.09 ± 0.15</b>	<b>1.25 ± 0.16</b>	0.49 ± 0.17
<b>Kidneys</b>	0.74 ± 0.09	1.10 ± 0.12	<b>4.96 ± 0.92</b>
<b>Liver</b>	<b>0.92 ± 0.09</b>	<b>1.50 ± 0.16</b>	0.44 ± 0.08
Lungs	0.35 ± 0.05	0.36 ± 0.05	0.17 ± 0.03
Lymphatic nodes	0.30 ± 0.04	0.27 ± 0.03	0.23 ± 0.06
Muscle	0.22 ± 0.04	0.15 ± 0.03	0.13 ± 0.04
Esophagus	0.41 ± 0.04	0.43 ± 0.03	0.20 ± 0.02
Oral mucosa	0.19 ± 0.03	0.11 ± 0.02	0.08 ± 0.03
Ovaries	0.27 ± 0.04	0.16 ± 0.03	0.12 ± 0.04
<b>Pancreas</b>	0.47 ± 0.04	0.59 ± 0.04	<b>0.63 ± 0.22</b>
Prostate	0.23 ± 0.04	0.13 ± 0.02	0.10 ± 0.04
Red bone marrow	0.30 ± 0.04	0.25 ± 0.04	0.21 ± 0.05
Salivary glands	0.18 ± 0.03	0.11 ± 0.02	0.07 ± 0.03
Skin	0.15 ± 0.02	0.11 ± 0.02	0.08 ± 0.02
Small intestine wall	0.27 ± 0.04	0.24 ± 0.04	0.31 ± 0.08
Spleen	0.60 ± 0.07	0.50 ± 0.07	0.46 ± 0.10
Stomach wall	0.41 ± 0.04	0.48 ± 0.05	0.36 ± 0.10
Testes	0.18 ± 0.03	0.10 ± 0.02	0.07 ± 0.03
Thymus	0.29 ± 0.04	0.25 ± 0.04	0.13 ± 0.02
Thyroid	0.22 ± 0.03	0.15 ± 0.02	0.09 ± 0.03
Urinary bladder wall	0.21 ± 0.03	0.13 ± 0.02	0.10 ± 0.03
Uterus/cervix	0.26 ± 0.04	0.15 ± 0.03	0.12 ± 0.04
Effective dose (mSv/MBq)	0.34 ± 0.03	0.35 ± 0.02	0.26 ± 0.05

**Supplemental Table 8. Biodistribution of the C4 radioligands in PD-L1<sup>+</sup> and PD-L1<sup>-</sup> human NSCLC xenograft models.**

Female nude mice bearing subcutaneous PD-L1<sup>+</sup> H1975 xenografts or PD-L1<sup>-</sup> A549 xenografts were injected with the C4 radioligands, and PET/CT scans were acquired at selected times post-injection. Image-derived radioligand tissue uptake was expressed as percentage of injected dose per volume of tissue (%ID/cm<sup>3</sup>). Data are presented as mean ± SD.

<b><sup>89</sup>Zr-IgG C4 (H310A/H435Q) uptake (%ID/cm<sup>3</sup>)</b>						
<b>N = 6 mice per model</b>						
<b>Time post-injection</b>		<b>1 h</b>	<b>4 h</b>	<b>24 h</b>	<b>48 h</b>	<b>72 h</b>
Blood pool	H1975 model	20.70 ± 0.90	12.19 ± 0.66	2.22 ± 1.22	0.96 ± 0.53	0.71 ± 0.39
	A549 model	20.66 ± 0.90	11.20 ± 1.16	2.42 ± 1.33	1.11 ± 0.62	0.92 ± 0.51
Liver	H1975 model	11.84 ± 1.06	12.39 ± 0.61	12.00 ± 0.51	10.55 ± 0.38	10.66 ± 0.63
	A549 model	15.33 ± 0.68	19.19 ± 1.07	17.49 ± 0.93	13.12 ± 0.66	11.12 ± 1.20
Kidney	H1975 model	9.05 ± 0.21	5.49 ± 0.44	1.56 ± 0.86	1.05 ± 0.58	0.85 ± 0.47
	A549 model	9.20 ± 0.65	5.52 ± 0.41	1.42 ± 0.21	0.95 ± 0.53	0.99 ± 0.54
Spleen	H1975 model	7.35 ± 0.78	6.72 ± 0.49	3.81 ± 0.58	3.09 ± 0.49	3.24 ± 1.77
	A549 model	7.76 ± 0.56	7.00 ± 0.28	3.97 ± 0.29	2.75 ± 0.40	2.68 ± 0.37
Tumor	H1975 model	1.48 ± 0.15	3.92 ± 0.51	4.60 ± 0.39	3.48 ± 0.33	2.69 ± 0.27
	A549 model	0.93 ± 0.11	1.86 ± 0.17	2.27 ± 0.30	1.51 ± 0.33	1.34 ± 0.64
Muscle	H1975 model	0.72 ± 0.06	0.79 ± 0.06	0.49 ± 0.05	0.43 ± 0.06	0.39 ± 0.03
	A549 model	0.71 ± 0.06	0.77 ± 0.04	0.50 ± 0.07	0.40 ± 0.05	0.35 ± 0.16
<b><sup>89</sup>Zr-Fab C4 uptake (%ID/cm<sup>3</sup>)</b>						
<b>N = 5-6 mice per model</b>						
<b>Time post-injection</b>		<b>1 h</b>	<b>4 h</b>	<b>24 h</b>	<b>48 h</b>	<b>72 h</b>
Blood pool	H1975 model	6.48 ± 2.74	0.86 ± 0.48	0.19 ± 0.11	0.12 ± 0.07	0.11 ± 0.06
	A549 model	5.10 ± 1.11	1.45 ± 0.81	0.32 ± 0.18	0.16 ± 0.09	0.14 ± 0.08
Liver	H1975 model	2.90 ± 0.31	1.46 ± 0.07	1.02 ± 0.13	0.90 ± 0.41	0.83 ± 0.38
	A549 model	2.68 ± 0.39	1.76 ± 0.21	1.58 ± 0.17	1.33 ± 0.14	1.27 ± 0.18
Kidney	H1975 model	69.57 ± 28.48	64.91 ± 4.50	40.08 ± 0.99	29.58 ± 13.40	22.76 ± 10.20
	A549 model	76.44 ± 3.59	67.26 ± 5.36	46.97 ± 3.97	35.16 ± 3.88	27.58 ± 4.24
Tumor	H1975 model	1.06 ± 0.12	1.36 ± 0.11	0.79 ± 0.12	0.59 ± 0.26	0.50 ± 0.23
	A549 model	0.62 ± 0.06	0.65 ± 0.27	0.39 ± 0.17	0.30 ± 0.14	0.23 ± 0.12
Muscle	H1975 model	0.54 ± 0.08	0.22 ± 0.02	0.14 ± 0.02	0.13 ± 0.06	0.12 ± 0.05
	A549 model	0.39 ± 0.03	0.23 ± 0.10	0.16 ± 0.07	0.14 ± 0.06	0.10 ± 0.05